

**FABRICATION AND CHARACTERIZATION
OF LAYERED SPHERICAL
INFRARED FILTER PARTICLES**

by

Benjamin Siddhartha Garrett

A thesis submitted to the Faculty of the University of Delaware in partial fulfillment of the requirements for the degree of Master of Science in Electrical and Computer Engineering

Spring 2017

© 2017 Benjamin S. Garrett
All Rights Reserved

**FABRICATION AND CHARACTERIZATION
OF LAYERED SPHERICAL
INFRARED FILTER PARTICLES**

by

Benjamin Siddhartha Garrett

Approved: _____
Mark S. Mirotznik, Ph.D.
Professor in charge of thesis on behalf of the Advisory Committee

Approved: _____
Kenneth E. Barner, Ph.D.
Chair of the Department of Electrical and Computer Engineering

Approved: _____
Babatunde A. Ogunnaike, Ph.D.
Dean of the College of Engineering

Approved: _____
Ann L. Ardis, Ph.D.
Senior Vice Provost for Graduate and Professional Education

ACKNOWLEDGMENTS

I would like to, firstly, thank my advisor, Dr. Mirotznik aka Big Dog, for the opportunity to continue my studies in electrical engineering, for his guidance and expression of wisdom throughout my research. I would like to thank my bud Nick Hudak for his tremendous help in these experiments and daily motivation. I would like to thank the team at Lumilant, Dr. Sharkawy, Dr. Zablocki, and Dr. Creazzo for sharing some of their knowledge on electromagnetic filter theory and fabrication techniques. I would like to thank everyone in the lab group for keeping a light but productive atmosphere, which encouraged a determined and progressive workflow. I would like to, in general, thank anyone who has answered any question or helped in any problem that I had throughout this journey. Lastly, of course, I thank my family.

TABLE OF CONTENTS

LIST OF TABLES	vi
LIST OF FIGURES.....	vii
ABSTRACT	x

Chapter

1	INTRODUCTION TO ELECTROMAGNETIC FILTERS.....	1
1.1	Motivation	1
1.2	Planar Reflectors and Filters	2
1.3	Mie Theory in Brief.....	5
2	MATERIAL SELECTION.....	11
2.1	Complex Refractive Index.....	11
2.2	Substrates.....	13
2.2.1	Small Particles and Van der Waals Forces	16
2.3	Deposition Materials	18
3	SPUTTERING SYSTEM FOR FABRICATION	21
3.1	Fundamentals of Sputtering Process	21
3.2	Modifications to Denton Discovery 18	22
3.3	Sieving.....	26
3.4	Fluidization Mechanism	28
3.5	Sputtering Process Parameters	35
4	CHARACTERIZATION.....	36
4.1	Materials Characterization Methods.....	36
4.1.1	SEM Microscopy.....	36
4.1.2	EDS Analysis.....	37
4.2	Silicon on Silicon Dioxide Microspheres.....	39
4.2.1	250 μ m Silicon Dioxide Spheres.....	39
4.2.2	2 μ m Silicon Dioxide Microspheres.....	41
4.2.2.1	TEM Analysis of 2 μ m Spheres	43
4.2.2.2	Mixing in 40 μ m Spheres into 2 μ m Spheres.....	44

4.3	Planar Deposition Rate	47
4.4	Aluminum Study	48
4.4.1	Sample Preparation Process and Fabrication Parameters.....	49
4.4.2	SEM Imaging.....	49
4.4.3	nanoComposix Generated Mass Extinction Spectrum Profiles...	65
5	CONCLUSION AND FUTURE DIRECTION.....	71
5.1	Summary.....	71
5.2	Future Works	71
	REFERENCES	72

LIST OF TABLES

Table 2.1 List of substrates used throughout series of experiments.....	14
Table 3.1: List of typical sputter parameters, values may change for special experiments or based on fluidization of particles.....	35
Table 4.1: List of useful critical excitation energies for EDS Analysis	38
Table 4.2: Sample description of six samples prepared for nanoComposix analysis ..	48
Table 4.3: Aluminum study parameters (nanoComposix provided)	66

LIST OF FIGURES

Figure 1.1: Bragg reflector showing the construction of waves as it interacts at each interface for a 3 layer structure.....	3
Figure 1.2: The reflectance $ \Gamma ^2$ for a Silicon, Silicon-Dioxide seven layer stack	4
Figure 1.3 Extinction efficiency vs. size parameter for a homogeneous sphere as shown in [3].....	6
Figure 1.4: Various Qext plots for a latex sphere $N_s=1.59$ with differing surrounding medium refractive indices [3]	8
Figure 2.1: Amorphous Silicon's complex index of refraction centered around its bandgap energy corresponding wavelength 1.117 μ m, n-red, k-blue.	12
Figure 2.2: Amorphous Silicon's complex index of refraction centered about its bandgap energy 1.11 eV, n-red, k-blue.	13
Figure 2.3: Complex index of refraction for Silicon Dioxide	15
Figure 2.4: Complex index for Aluminum, n-red, k-blue.	19
Figure 3.1 Cryopump arm assembly	25
Figure 3.2: Humboldt Sieve shaker with several sieved secured on top of the spouted catching pan	27
Figure 3.3: Gear motor and internal drive shaft assembly.	29
Figure 3.4: Instrumentation for generating and measuring voltage delivered to the electromagnetic shaker	30
Figure 3.5: Side cross section view of final particle cup.....	31
Figure 3.6: Rod assembly	32
Figure 3.7: Particle comb and collar.....	33
Figure 4.1: An uncoated 197 μ m SiO ₂ microsphere	39
Figure 4.2: 26 hours of Silicon deposition on a 250 μ m SiO ₂ sphere	40
Figure 4.3: InLens (left) and ESB (right)	41

Figure 4.4: Silicon coated 2 μ m SiO ₂ microsphere	42
Figure 4.5: TEM of entire 2 μ m after 7.5 hours of Silicon deposition.....	43
Figure 4.6: TEM of edge of 2 μ m after 7.5 hours of Silicon deposition.....	44
Figure 4.7: 1.25g of 40 μ m spheres mixed into 3.75g of 2 μ m sputtered with Silicon for 4 hours	45
Figure 4.8: Cross section of a 2 μ m sphere from mix	46
Figure 4.9: Planar deposition for rate estimation	47
Figure 4.10: Uncoated hollow glass microspheres.....	50
Figure 4.11: 8 hours of Aluminum deposition on several hollow SiO ₂ spheres	51
Figure 4.12: 8 hours of Aluminum deposition on a larger hollow SiO ₂ microsphere..	52
Figure 4.13: 8 hours of Aluminum deposition on a smaller hollow SiO ₂ microsphere	53
Figure 4.14: EDS line scan of 8 hour Aluminum deposition on hollow SiO ₂ microsphere surface.....	54
Figure 4.15: Surface morphology of 24 hour Aluminum coating on hollow glass microsphere	55
Figure 4.16: Cross sectional view of a 24 hour Aluminum coated hollow SiO ₂ microsphere via InLens detection.....	56
Figure 4.17: Cross sectional view via SESI (left) and ESB (right) detection methods	56
Figure 4.18: EDS Image of 24 hour Aluminum coated hollow SiO ₂ microsphere	57
Figure 4.19: Uncoated HDPE.....	58
Figure 4.20: 4 hour aluminum on HDPE.....	59
Figure 4.21: EDs mapping of 4 hour Aluminum deposition on a HDPE microsphere	60
Figure 4.22: Surface morphology of a 24 hour Aluminum deposition on HDPE.....	61
Figure 4.23: EDS of 24 hour Aluminum deposition on HDPE.....	62

Figure 4.24: EDS of detected elements on sample #6.....	62
Figure 4.25: SEM of 24 hour Aluminum coating on HDPE microthene sphere cross section.....	63
Figure 4.26: EDS of 24 hour Aluminum coating on HDPE microthene sphere cross section.....	64
Figure 4.27: Timed Aluminum deposition onto hollow SiO ₂ microspheres	67
Figure 4.28: MEC of timed Aluminum deposited onto HDPE microthene microspheres.....	68
Figure 4.29: Polyethylene transmission spectrum sourced from [19] for comparison to engineered particles.....	69

ABSTRACT

The ability to deposit layers of optical material on to micro-spherical particle substrates yields interesting and optimal electromagnetic mass extinction and other Mie theory scattering spectrum properties. Microsphere particle infrared filters, for use within the near-infrared/short-wavelength infrared (NIR/SWIR, $\lambda=1\mu\text{m}$ to $3\mu\text{m}$) and long-wavelength infrared (LWIR, $\lambda=8\mu\text{m}$ to $12\mu\text{m}$) spectral bands can be engineered by selecting materials with specific geometries and wavelength dependent complex refractive indices that tailor to desired mass extinction spectrum characteristics.

Infrared filters that are lightweight and possess isotropic geometries, namely microspheres, are extremely valuable in many atmospheric science related applications. However, the applications certainly do not stop there; some other examples include use in diffusive blended inks and paints. Computationally, it has been shown that engineered particles possess superior wavelength specific mass extinction properties than many other infrared particle filters in existence currently.

In this thesis, the method of fabrication of such layered microsphere particles will be detailed. Through renovation and modification of a radio frequency magnetron sputtering system layers were able to be deposited on to micro-spherical substrates with measurable layer thicknesses. Results of characterization will also be shown. Furthermore, future directions and other applications will also be discussed.

Chapter 1

INTRODUCTION TO ELECTROMAGNETIC FILTERS

1.1 Motivation

Tunable electromagnetic filters for specific bands especially within NIR/SWIR and LWIR bands are of great interest to electrical engineers for applications such remote atmospheric sensing technologies, diffusive paints and blending inks, and much more. It has been theorized and computationally proven that infrared tunable notch filters and band attenuation filters can be designed by optimizing core microsphere substrate material and diameter along with stratified layer material and thickness on the order of nanometers. Custom Matlab code parallel to this thesis has produced several sphere specifications for various electromagnetic Mie extinction and scattering spectral responses. Efforts to achieving the goal, to realize these designed particles through the means of physical deposition methods namely magnetron RF sputtering, have proven to be novel and challenging, but overall have produced interesting results.

This thesis will explore the development of engineered microspherical filters for the advantage of isotropy, the hopes of surpassing existing mass extinction coefficient values, and creating filter bands by manipulating constitute materials and their geometries.

1.2 Planar Reflectors and Filters

Before assuming that optical filters and high efficiency scatterers can be made from spherical geometries it is important to first verify that filters and reflectors can be made from planar geometries. The conversion from Cartesian to spherical coordinate systems can be made relatively easily and is necessary to apply Maxwell's equations to the appropriate boundary value problem.

One of the most studied reflectors in the electromagnetics community is the Bragg reflector. The Bragg reflector is made of alternating high and low indexed dielectric materials arranged so that the high index layers are the outermost on either side of the reflector. Each layer is a quarter wavelength ($\lambda/4$) in thickness. The wavelength that is used for the layer thickness calculation is the wavelength for the given medium, λ/n , n denoting the real part of the index of refraction. For optimum reflection, the layer thicknesses are tailored to the center frequency of the total band of electromagnetic energy to be reflected. The reflection of a single interface is simply

$$\Gamma = \frac{n_1 - n_2}{n_1 + n_2} \quad (1.1)$$

From this it is apparent that if the index in the second material, n_2 , is greater than the index in the first material, n_1 , there will be a negative multiplier to the amplitude of the reflected wave. An incident wave to the multilayer dielectric mirror experiences a 180 degree phase shift as it is reflected by the first boundary from low indexed surrounding medium to the high index of the first layer. Some portion of the incident wave is transmitted through the interface and experiences another 90 degree phase change due to the $\lambda/4$ distance it has to travel through the dielectric. At the end of this $\lambda/4$ travel at the next interface from high to low index the reflection results in a positive value, corresponding to a 0 degree phase shift. This process of change of

phase of the incident, transmitted and reflected waves is repeated for the number of layers applied to the dielectric stack, as long as there are an odd number of layers with the higher index on the outsides. These phase changes result in an in-phase construction of all of the reflected waves that made it back to the original medium, resulting in one coherent reflected wave. As the wavelength deviates from the center wavelength deconstruction starts to occur and reflection is less effective [1].

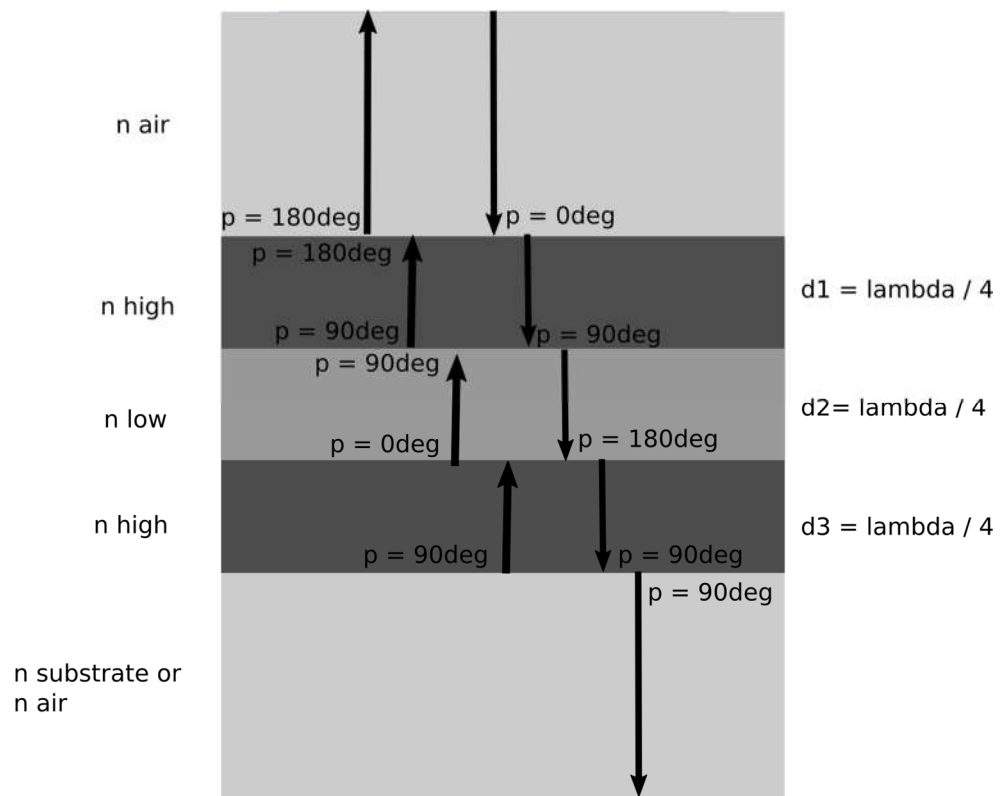


Figure 1.1: Bragg reflector showing the construction of waves as it interacts at each interface for a 3 layer structure

Professor S. Orfandis has developed a code that calculates the reflectance, Γ , for a stack of dielectrics [2]. The user inputs a range of wavelengths in units of the center wavelength, λ_0 , the layer thicknesses in units of the center wavelength, and the index of refraction for each of the layers plus the index of the surrounding medium. Quick experimentation of this code shows that there is a reflectance resonance around the center wavelength and reflection decreases gradually away from the center wavelength. For this example, the evaluated wavelengths range from 1 to 10 μm with a center wavelength of 5 μm . The stack is composed of seven layers of alternating index of refractions of 3.42 and 1.34 to represent Silicon and Silicon Dioxide respectively at 5 μm wavelength, with Silicon on either ends of the stack. An index of 1.0 to represent air surrounds the structure. Each layer is a quarter of the center wavelength in thickness.

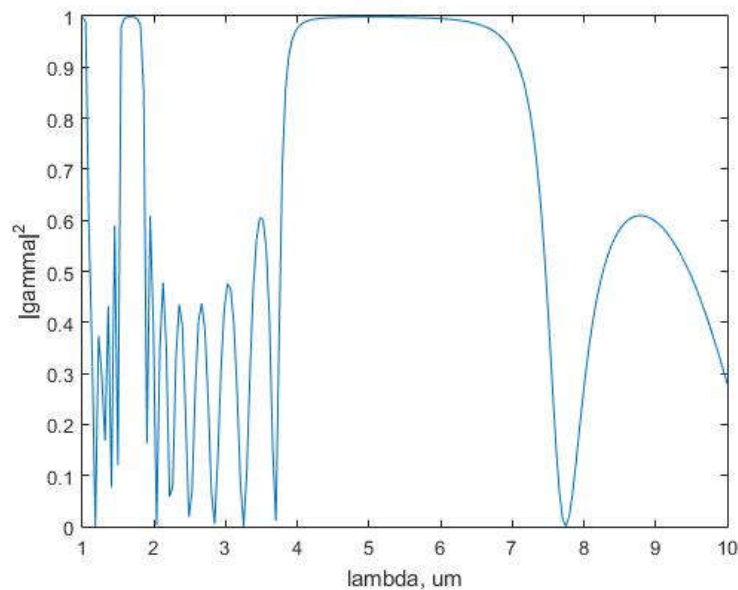


Figure 1.2: The reflectance $|\Gamma|^2$ for a Silicon, Silicon-Dioxide seven layer stack

Another interesting structure is the antireflective coating. This relies on deconstruction of reflected wave as opposed to in phase construction of the Bragg reflector. In this case, there is one layer between the surrounding medium, usually air and the substrate. This coated layer is also a quarter wavelength in thickness but the index and is optimally chosen to be the square root of the index of the surrounding medium and the index of the substrate. The geometric mean minimizes the amount of reflection.

Given these two examples, it is apparent that optical filters are physically realizable. The question now, is there angle dependences for these structures. For a quarter wavelength planar structure: turning it so that the incoming wave is obliquely incident, geometrically the incident wave will see a longer optical path. The optical length will transform to an elongated distance of $\lambda/4/\cos\theta_i$. This has negative effects on the electromagnetic filter properties, if one is attempting to create a robust isotropic filter. The solution is to provide the means to fabricate spherical isotropic filters.

1.3 Mie Theory in Brief

Mie theory describes the Mie/Lorenz-Mie solution to Maxwell's equations for scattering of an incident electromagnetic wave by a sphere. The parameters that are of most interest produced through Mie theory are the efficiency coefficients for absorption (Q_a), scattering (Q_s), and extinction (Q_e) as reviewed in [3]. The efficiency of extinction is the sum of the efficiency of scattering and the efficiency of absorption

$$Q_e = Q_s + Q_a \quad (1.1)$$

The extinction efficiency is computed by the following

$$Q_e = \frac{2}{x^2} \sum_{j=1}^{\infty} (2j + 1) \text{Re}(a_j + b_j) \quad (1.2)$$

Likewise, the scattering is computed by

$$Q_s = \frac{2}{x^2} \sum_{j=1}^{\infty} (2j + 1)(|a_j|^2 + |b_j|^2) \quad (1.3)$$

The absorption efficiency is the difference between the extinction efficiency and the scattering efficiency, $Q_a = Q_e - Q_s$. The variable x is called the diffraction parameter otherwise known as the size parameter, it is calculated only in the surrounding medium, and is equated by

$$x = \frac{2\pi a}{\lambda} \quad (1.4)$$

Where a is the diameter of the sphere. The size parameter is the relation of the size of the sphere to the wavelength. In general, the scattering, absorption and thus extinction efficiencies peak when the diameter of the sphere and the wavelength are equal.

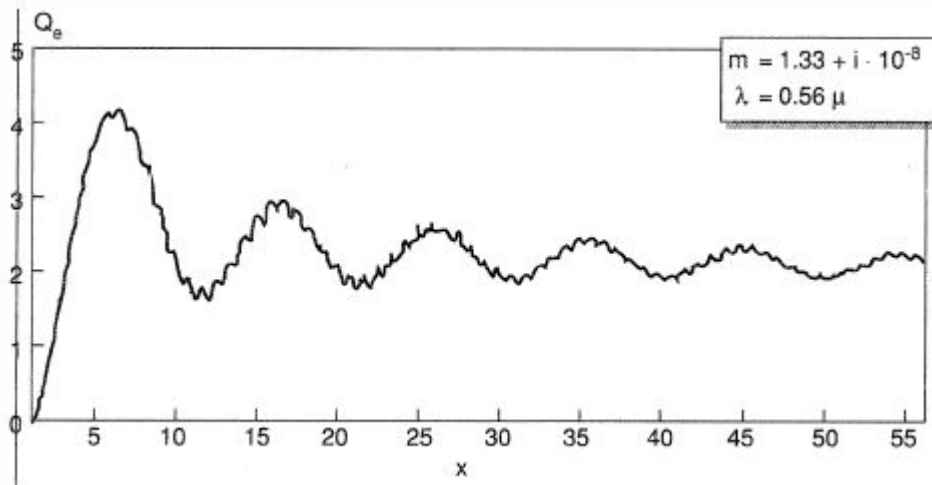


Figure 1.3 Extinction efficiency vs. size parameter for a homogeneous sphere as shown in [3]

In the region, which the diameter of the particle is much smaller than wavelength of light, the size parameter x much less than unity, the scattering is approximated to Rayleigh scattering. Extinction is very low here and has little use for engineering electromagnetic filters. When the diameter equals the wavelength, x equates to 2π , which produces the strongest resonance of extinction by means of scattering and absorption of incident plane waves on to the sphere. The constitute expansion coefficients a_j and b_j describe the fields external to the sphere and are composed of Riccati-Bessel functions $\psi_j(t)$ and $\xi_j(t)$. Where

$$a_j = \frac{\left\{ \psi_j(x) \left[\frac{\psi'_j(m_\lambda x)}{\psi_j(m_\lambda x)} \right] - m_\lambda \psi'_j(x) \right\}}{\left\{ \xi_j(x) \left[\frac{\psi'_j(m_\lambda x)}{\psi_j(m_\lambda x)} \right] - m_\lambda \xi'_j(x) \right\}} \quad (1.5)$$

$$b_j = \frac{\left\{ m_\lambda \psi_j(x) \left[\frac{\psi'_j(m_\lambda x)}{\psi_j(m_\lambda x)} \right] - \psi'_j(x) \right\}}{\left\{ m_\lambda \xi_j(x) \left[\frac{\psi'_j(m_\lambda x)}{\psi_j(m_\lambda x)} \right] - \xi'_j(x) \right\}} \quad (1.6)$$

and,

$$\psi_j(\rho) = \rho j_n(\rho) \quad (1.7)$$

$$\xi_j(\rho) = \rho h_n^1(\rho) \quad (1.8)$$

The Riccati-Bessel function $\xi_j(\rho)$ is composed of the outward traveling spherical Bessel function of the third kind, otherwise known as spherical Hankel function. Both $\psi_j(\rho)$ and $\xi_j(\rho)$ are proportional to the distance ρ from the center of the sphere.

These equations assume nonmagnetic materials, and the magnetic permeability, μ_r , of the medium and sphere are equated to unity throughout this thesis.

These efficiencies are physically meaningful quantities. They represent the relation of the electromagnetic cross section to the physical cross section.

$$Q_i = \frac{\sigma_i}{\pi r^2} \quad (1.9)$$

For a particular efficiency Q_i , σ_i is the electromagnetic cross section and is wavelength dependent due to the material properties of the sphere.

The smaller oscillations superimposed onto the lower frequency on the Q_{ext} vs x graph in the figure above are due to mismatch of refractive index between the medium and of the sphere. In Ng's dissertation's Chapter 3 Mie Theory [4] several mediums with similar spheres' extinction efficiency graphs were plotted.

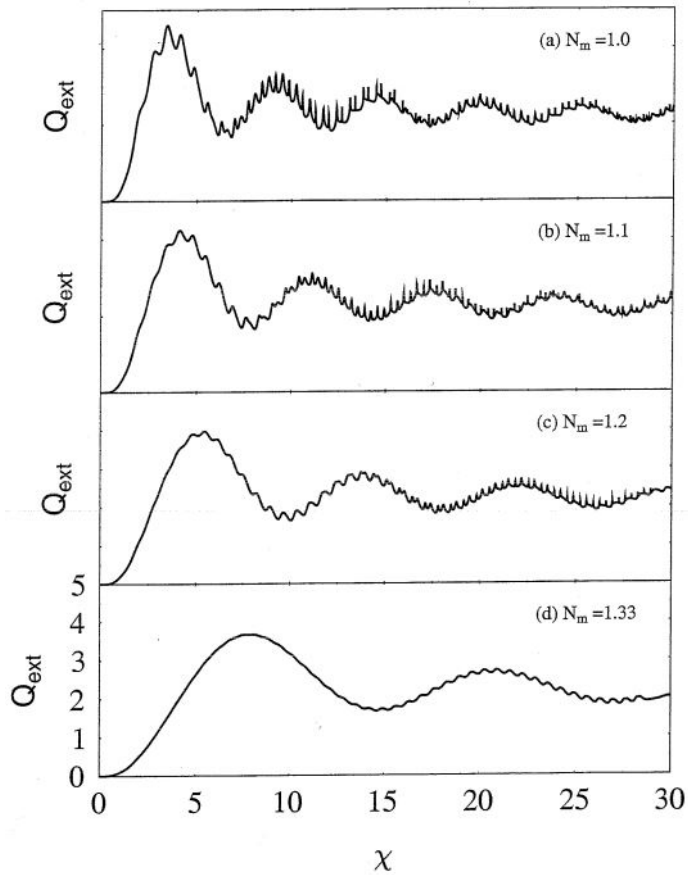


Figure 1.4: Various Q_{ext} plots for a latex sphere $N_s=1.59$ with differing surrounding medium refractive indices [3]

From the figure above it is understood that a larger discrepancy between the index of the sphere, N_s , and of the medium, N_m , produces more of the higher frequency oscillations superimposed to the overall Q_{ext} waveform. In terms of optimization of simulation results, this was considered when choosing geometries and materials for filtering effects thus affecting the materials to use for physical fabrication. The oscillations provide the means for passband and stopband filter characteristics for any given sphere.

From the extinction efficiency coefficient, the mass extinction coefficient is derived by the formula

$$\alpha = \frac{Q_e(\pi a^2)}{M_{\text{particle}}} = \frac{\sigma_e}{M_{\text{particle}}} \quad (1.10)$$

The mass extinction coefficient holds units of area divided by mass. Often, mass extinction coefficient is of prime interest and has the most physical meaningfulness for qualitative comparison between scattering particles. Not only can the mass extinction coefficient be increased by optimizing choice of materials based on optical properties it can also be enhanced by choosing relatively lightweight materials. A low density core material or no core at all can result in high mass extinction coefficient values.

The mass extinction coefficient is then used to calculate the total transmittance through a length of a mass concentration c of particles by Beer-Lampart Law formula

$$T = \frac{I(L)}{I_o} = e^{-\alpha c L} \quad (1.11)$$

With a reliable transmittance measuring method such as a Fourier Transform Infrared Spectrometry (FTIR) and with careful accounting of the mass concentration of spheres to background material, the mass extinction coefficient can be backed out from the given transmittance. Rearranging transmittance given from an FTIR yields.

$$\alpha = -\frac{\ln(T)}{cL} \quad (1.12)$$

Likewise, the mass extinction coefficient can be related to absorbance by the following.

$$\alpha = 2.3 \frac{A}{cL} \quad (1.13)$$

The purpose of introducing the equations governing Mie scattering is to show appreciation to the theoretical background that went into formulating designs to later realize and characterize.

Chapter 2

MATERIAL SELECTION

2.1 Complex Refractive Index

The complex refractive index, mentioned in previous sections, is an opto-electromagnetic property that describes how an electromagnetic wave travels through a given material. The equation $m = n + ik$ defines the complex refractive index. The real part n can simply be called the index of refraction, or index, and it describes the phase velocity and how the wave refracts at the boundary interface between materials. The relationship between the velocity of a wave in free space vacuum and within a material is given by, $n = c/v$. Where c is the speed of light in a vacuum being approximately 2.998×10^8 meters per second, and v is the phase velocity of light in the material. The imaginary part, k , is called the extinction coefficient and describes the rate of attenuation of the wave through the material. Both the index of refraction and the extinction coefficient are functions of wavelength. Generally, for pure elements, the extinction coefficient is negligible for wavelengths that correspond to an energy less than the bandgap of the material. For compound molecules, the extinction becomes more involving since the number of elements included introduce additional allowable energy states and other resonance phenomena within the medium. To understand how wavelength and energy are related it is required to state Plank's equation, which is $E = hc/\lambda$. Where h is Plank's constant equal to 6.63×10^{-34} J-s. From Plank's relationship, we see that energy and wavelength are inversely proportional. For example, silicon's bandgap is 1.11 eV, which corresponds to a wavelength of $1.117 \mu\text{m}$. For photon energies less than the bandgap, at longer wavelengths, photons do not produce the excitement needed for electrons from the

lower energy valence band of the material's constituent atoms to quantum jump to the higher energy conduction band. However, for wave energies greater, which corresponds to shorter wavelengths, there is enough excitement and the absorption increases. This phenomenon is observed in well-documented extinction coefficients of many materials. Silicon is one of the most useful and an example of its index is shown here below [9].

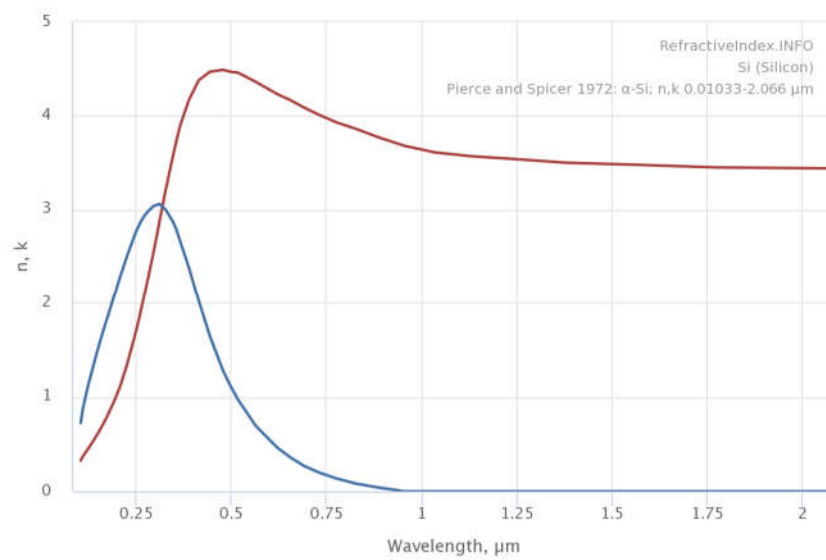


Figure 2.1: Amorphous Silicon's complex index of refraction centered around its bandgap energy corresponding wavelength 1.117μm, n-red, k-blue.

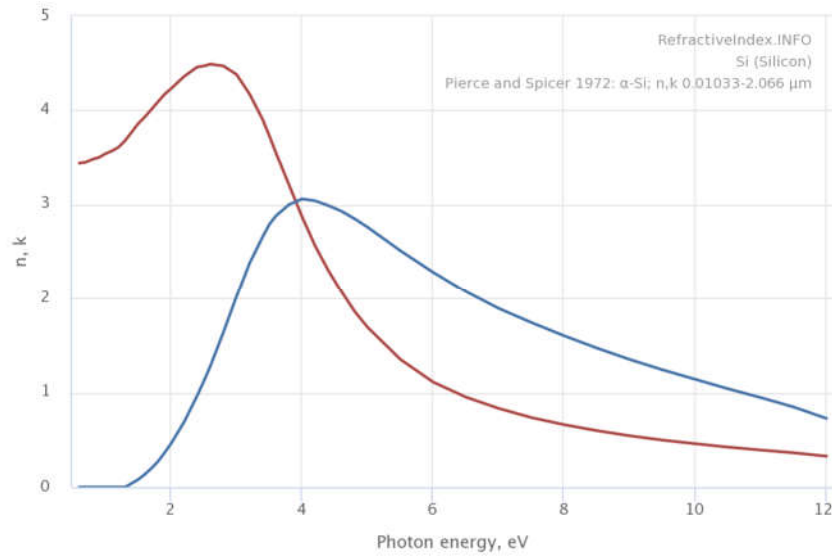


Figure 2.2: Amorphous Silicon’s complex index of refraction centered about its bandgap energy 1.11 eV, n-red, k-blue.

From the figures from [9], the decision of choosing a material that might be a good prospect for a good absorber is made a little more simply. The wavelength dependent complex refractive index was fully taken into account in the computational simulation of the obscurant extinction efficiency, mass extinction coefficient, and other scattering properties.

The complex index of refraction, m , contributes to the expansion coefficients, a_j and b_j . Therefore, extinction efficiency, mass extinction coefficient and overall transmission is dependent on m as well.

2.2 Substrates

Relatively precise and cost effective microsphere substrates are available on the market for purchase. However, there are also many ultra precise monodispersed microspheres listed for hundreds of dollars for mere milliliters of material. Many of

these options were out of a reasonable price range. In purchasing microspheres sometimes the stringent need for exact desired dimensions to meet that of the simulated model had to be relaxed. Many times, even though the manufacturer claimed that the substrate was within a certain diameter range, in house characterization showed a more polydispersed size distribution from particle to particle in a newly purchased sample.

The substrates that were used throughout experiments related to this thesis include many Silicon-Dioxide (SiO_2) microspheres along with some high density polyethylene (HDPE) “microthene” microspheres. Several diameters of spheres were experimented with for deposition. Though the table below shows the exhaustive list of substrates tried, many of these substrates were used mainly for fluidization experimentation and deposition experimentations that did not yield meaningful information to characterize the methods of fabrication, but rather, just to gain a better intuition going forward to specific designs.

Table 2.1 List of substrates used throughout series of experiments

Substrate#	Material	Expected Size	Source
1	SiO_2	250 μm	Amazon
2	SiO_2	40-70 μm	Corpusular
3	SiO_2	15-40 μm	Corpusular
4	SiO_2	10-25 μm	Corpusular
5	Hollow SiO_2 Shell	9-13 μm	Sigma-Aldrich
6	SiO_2	2 μm	Superior Silica
7	HDPE	20 μm	LyondellBasell

Substrates for characterization driven experiments included silicon dioxide (SiO_2) solid and hollow glass microspheres and high density polyethylene (HDPE,

microthene) microsphere-particles. Glass microspheres with a diameter of $2\mu\text{m}$ were purchased from the manufacturer Superior Silica. Hollow glass microspheres with a claimed diameter of $9\mu\text{m}$ to $13\mu\text{m}$ were purchased from the supplier Sigma-Aldrich. The microthene particles acquired are a LyondellBasell product. Large sandblasting media for initial fluidization testing was acquired a source through Amazon.com.

Many of the substrates used are of SiO_2 , below shows the complex refractive index of glass for the wavelengths of interest based on the Handbook of Optical constants of Solids [10].



Figure 2.3: Complex index of refraction for Silicon Dioxide

From this plot of complex index of refraction of Silicon Dioxide, it is apparent that it is dispersive. The real part, n , varies regularly from the short wave to long wave infrared. One discerning feature of SiO_2 is the strong absorption, k greater than 0.5, in the $8\mu\text{m}$ to $10\mu\text{m}$ wavelength band from the [8].

2.2.1 Small Particles and Van der Waals Forces

Van der Waals forces between the smaller 2 μm silica microspheres became quickly obvious soon after initial experimentation. The attractive forces between the particles possessing a high surface area to volume hindered the fluid mechanics necessary to perform uniform deposition of layers without any further processing. Van der Waals forces start to become more prominent over gravitational forces as the particle size become very small. Particles with a largest feature size of under a 100 μm are subject to agglomeration due to van der Waals forces. The basis of the forces are on a molecular level where the electronic configuration of the molecule of a material are such that there is net dipole characteristic according to Visser [11]. London van der Waal found the energy between two molecules to be

$$V = -\frac{3}{4} h v_0 \frac{\alpha^2}{d^6} \quad (2.1)$$

Where h equals Planks constant, α represents the polarizability, v_0 the characteristic frequency with a separation distance d [11]. Hamaker [12] went on to claim that molecular interactions are additive and scale to beyond the molecular level to the body itself and expressed the force between two semi-infinite bodies to be

$$P = \frac{A}{6\pi H^3} \quad (2.2)$$

Where A is the Hamaker coefficient based on the materials and H is the separation between them. In Hamaker's paper [12] he states an energy between two spherical particles in term of a function based on geometric information such as diameters, separation distance and on material properties as

$$E = -\pi q \lambda \frac{1}{6} \left\{ \frac{2R_1 R_2}{C^2 - (R_1 + R_2)^2} + \frac{2R_1 R_2}{C^2 - (R_1 - R_2)^2} + \ln \left(\frac{C^2 - (R_1 + R_2)^2}{C^2 - (R_1 - R_2)^2} \right) \right\} \quad (2.3)$$

Where R_1 and R_2 are radii, C is the separation of the centers, q is the atom density and λ is the London van der Waals constant. This constant between two particles is expressed as.

$$\lambda = \frac{3}{2} \alpha_k \alpha_l \frac{I_k I_l}{I_k + I_l} \quad (2.4)$$

Where λ is in units of erg-cm⁶, α is the polarizability of the atoms and I is the certain characteristic potential of the atoms.

Without calculating the actual forces between individual particles methods to fluidize to effectively break apart most of the agglomerates were used during depositions to be covered in more detail in later sections. Van der Waals forces were a major challenge throughout this thesis and were addressed by means of mechanical fluidization. Mechanical fluidization of the microspheres had a greater effectiveness on larger diameter microspheres but also showed to have some success on mixing 2 μ m particles so that deposited material was visually evident throughout the sample.

Geldart powder classification groups particles in to four classes A, B, C, and D based on size and fluidization behaviors [11]. Group A, aeratable particles are between 20 and 100 μ m in diameter with a particle density usually below 1.4g/cm³. Group B, sand like particles are between 40 and 500 μ m in diameter and usually have densities between 1.4 and 4g/cm³. Group C, cohesive particles are less than 20 μ m in diameter, with density differences greater than 1g/cm³. Finally, group D, spoutable particles with diameters of greater than 600 μ m. The particles presented in this thesis are technically classified in to the groups A, B, and C. No experimentations were done on particles larger than about 250 μ m in diameter.

2.3 Deposition Materials

The materials for deposition tests consisted of Silicon, and Aluminum. In the case for Silicon, it along with alternating layers of Silicon Dioxide is capable of producing tunable pass band filters utilizing spherical substrates. In the case for Aluminum, it is possible to create strong band attenuators out of lightweight particles to yield a high mass extinction. These materials were chosen for their ease of use in a sputtering environment and for their ideal simulation responses. Both target materials were acquired from Kurt J. Lesker Company. The cathode head of the Denton Discovery 18 is a 3" diameter mounting, all of the targets used were ordered to fit this mount.

The Silicon targets that were used had the following properties. The material was p-type silicon with a resistivity of 0.005-0.020 ohm-cm, and 99.999% pureness. The size of the target was 3.00" in diameter by 0.125" in thickness. The target was indium bonded to a copper back plate. The purpose of indium bonded copper back plates is to provide better transfer of thermal energy between the cathode head and the target. The softer indium solder allows for some give between dielectric or semiconductor materials, in this case silicon, and the metal copper back plate to alleviate stress during thermal expansion of the materials, during the ramping of power up and down from the RF source. The indium bonded copper back plate reduces cracking due to a mismatch in thermal expansion coefficients [13].

The Aluminum targets that were used had the following properties. The material was 99.9995% pure with machined faces. The size of the target was 3.00" in diameter by 0.125" in thickness. It is not necessary to apply an indium bonded copper back plate to aluminum. This is because the cathode head is constructed from copper, the thermal and electrical conductivities of copper and aluminum are close enough that

cracking due to thermal expansion are not an issue as long as proper power ramp up and ramp down procedures and precautions are followed carefully. However, it is possible to warp an aluminum target if the power from the RF source suddenly experiences a great drop by some sort of fault in operation, either user or facility generated.

As discussed previously index of refraction plays a crucial role for material selection. Aluminum was chosen for its significant absorption of infrared.

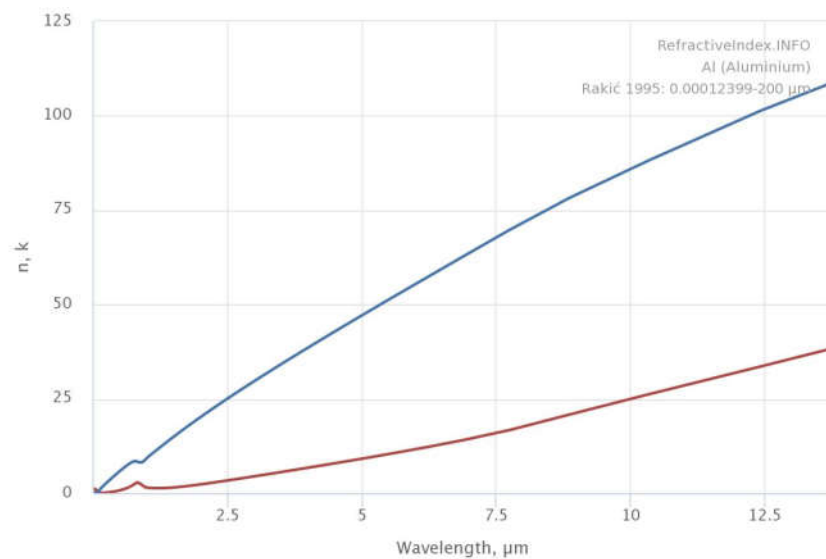


Figure 2.4: Complex index for Aluminum, n-red, k-blue.

Both the real and the imaginary parts of the index quickly increase as wavelength increases. The high extinction coefficient, k , corresponds to a shallow skin depth which is found by Sigel []

$$\delta_e = \frac{\lambda}{2\pi k} \quad (2.5)$$

The skin depth can also be found for a good conductor through the following Balanis [balanis].

$$\delta = \left(\frac{2}{\omega \mu \sigma} \right)^{0.5} \quad (2.6)$$

At a wavelength of 12 μm the skin depth turns out to be about 19.4nm. For engineering a strong absorber, a layer thickness of only a few multiples of this depth is necessary and is achievable through the developed deposition process.

Chapter 3

SPUTTERING SYSTEM FOR FABRICATION

3.1 Fundamentals of Sputtering Process

RF magnetron sputtering is a physical vapor deposition (PVD) method that offers great control of index of refraction and deposited layer thickness rates. It is capable of depositing many types of materials from electrical conductors to insulators by bombarding a target material with ions, usually of argon, which ejects target atoms on to the substrate. In the Denton Discovery 18 the cathode is located at the top of the chamber, classifying it as a top-down sputter system. This system has two sources, one capable of DC sputtering and the other capable of RF magnetron sputtering. The experiments throughout this thesis utilized the RF magnetron sputtering source of this system. It is advantageous and necessary to use RF magnetron sputtering over DC sputtering for dielectric materials. In a DC voltage environment a highly resistive dielectric mounted to the cathode would block current to the conductive cathode. This blockage would extinguish the plasma necessary for sputtering as explained by Burak [14]. This is avoided by using RF sputtering because a static charge is unable to build on the surface of the dielectric suggested by Hughes [15].

The detailed steps to the mechanism of RF sputtering are as follows. The chamber is initially pumped down first by a rough mechanical pump to about 1.5×10^{-3} Torr then to a high vacuum of at most 5×10^{-6} Torr to reduce atmospheric impurities and to increase the mean free path of the ejected target material. Process gas, usually Argon, is flowed into the chamber at a set rate, for example at 20 standard cubic centimeters per minute (SCCM). A process pressure of 5×10^{-3} Torr is established via control of a variable valve downstream towards the high vacuum pump. An alternating

current (AC) voltage is applied to the cathode at an RF frequency of 13.56MHz. A matching network circuit of variable capacitors, C_T and C_L are tuned in order to transfer power from the cathode to the plasma to be. Once a low power plasma, of about 20 watts (W), is initiated the matching circuit parameters of the circuit are manually adjusted again to minimize reflected power to $P_r=0W$ between the cathode and the plasma. The plasma's power is ramped up to the desired value at this point, usually to between 75W and 100W. The plasma consists of cations, positively charged, ionized argon, Ar^+ atoms and negatively charged particles, electrons or anions. During the negative cycle, electrons are emitted from the cathode and interact with the flowed in neutral argon, or other, process gas. The emitted electrons motion through a magnetic field gives them enough kinetic energy, about 15.7eV, to knock away an electron from the neutral argon atoms [16]. A permanent magnet behind the target is in place and induces the magnetic field parallel to the target to confine secondary electrons to the local area in a toroid path. The toroid path caused by the magnetic field allows for a longer path than if without and for a higher probability that the electrons will cause more ionization of the argon gas, supporting the plasma which is responsible for the sputtering. The positively charged Argon atoms are attracted to the negative voltage cycle of the cathode. The attraction leads to a physical collision of the Argon ions on to the target material which ejects on to the substrate below.

3.2 Modifications to Denton Discovery 18

Over the course of research, there has been many necessary modifications to the Denton Discovery 18 sputter system. The biggest change to the system itself has been the replacement of the high vacuum pump. Originally, an Adixen Alcatel ATP150 turbo molecular diffusion pump served as the high vacuum pump and was

attached to the bottom of the main chamber via a DN100 ISO-K flange. It was isolated from the chamber by a pneumatically controlled high vacuum valve integrated into the system controls. After several failures and attempts at repairs, it was decided to upgrade the pump in the interest of reducing down time and increasing pump down speed.

The superior alternative to the turbomolecular pump for this particular purpose is a cryogenic pump. The basic concept of a cryo pump is that it traps gases by condensing them on to a very cold surface. The cryopump consists of 80K array, 80K radiation shield, 15K array and cold station heaters, which are attached to a cold head, all inside of a vacuum vessel. Water and hydrocarbon vapors are condensed in the 80K array while nitrogen, oxygen, and argon are condensed in the 15K array. The 15K array traps Helium, Hydrogen and Neon, these gases are trapped in its specifically processed charcoal as described in the Brooks user manual [6]. The advantage of using a cryopump is that it is less susceptible to damage due to particulates. With the turbomolecular pump there are several stages of turbines with increasingly finer fins each spinning at high rotational speeds with very little clearance between them. If particles were to enter the turbines, they could cause friction and reduce the spinning of the blades. If enough particulate were to have entered the turbine at a time it could have potentially caused a chain reaction of fin displacement and eventually total destruction of the pump. Since there are fewer particulate sensitive parts within the cryopump, it proved to be a much more reliable option. The specific cryopump model that was incorporated into the system was a Cryo-Torr 8F pump acquired from Brooks Automation.

Along with the cryopump itself a compressor, motor controller and new water chiller was additionally integrated in to the system. The compressor and motor controller worked together to operate the cryopump. The compressor cycles high pressure Helium through components of the cold head such as the displacer-regenerator assembly, crank case, and motor housing. The expansion of the Helium in the displacer-regenerator assembly cools the first and second stage cold stations [6].

More water flow was required for the addition of the water cooled compressor. The existing ThermoFlex 1400 was upgraded to a ThermoFlex 5000. The new ThermoFlex 5000 provides 4.09 gallons per minute (GPM) which the compressor needs about 1.5 GPM leaving at least another 1.5 GPM for the cathodes.

In order to isolate the cryopump as much as possible from the vibration from the fluidization process, which will be covered in later sections, an arm assembly was designed to mount the cryopump off the side of the chamber via an existing load arm port. From the left side of the chamber is a 90 degree elbow, to a vibration dampener, to a reducer flange, to a VAT butterfly valve, to another reducer flange, and finally to the cryopump.



Figure 3.1 Cryopump arm assembly

From top to bottom, the specific flanges are the following. A manual gate valve is connected to the chamber by an ASA 1100x60 flange. The elbow is mounted to the manual gate valve via an ASA 1100x60 flange. The elbow connects to the vibration dampener via ISO 200-K flange. The vibration dampener connects to the first reducer via ISO 200-K. The first reducer connects to the VAT butterfly valve via ISO 200-F. The VAT butterfly valve connects to the second reducer via ISO 200-F. Finally the second reducer connects to the cryopump via ISO 200-K. A support frame

was built to hold up the assembly to reduce the strain on the vibration dampener and to keep the cryopump level.

The VAT butterfly valve is computer controlled through a software called Control Performance Analyzer (CPA) 3.0. RS-232 serial lines were fabricated to link the VAT valve to a nearby computer. Through the CPA software the user is able to initiate a “LEARN” function which teaches the VAT valve the chamber parameters that take in account the chamber volume, the process flow rate and the “ZERO” base pressure. The user can set a pressure for the VAT valve to automatically keep through minor adjustments or set a physical position for the valve to hold from 0 to 100% open. The position indicated as 0% however does not mean a vacuum seal, since the butterfly valve design leaves room for the movement of the valve and the sidewalls the manual gate valve that is located upstream to provide a vacuum seal between the cryopump and the main chamber. The VAT valve is also connected to a newly installed a-Baratron AA02A Heated Absolute Capacitance Manometer. This pressure sensor, horizontally to the side of the main chamber has a full range scale of 0.1Torr and is read by the VAT valve for control and display of the chamber pressure during processing.

3.3 Sieving

Microspheres are first prepared by going through a sieving process. This process is simple but has some quirks to it. Microspheres tend to stick to almost everything that they come into contact to; this does not exclude sieves or utensils used for handling the spheres. Several sieves were acquired for the range of sizes of particles. These include individual sieves with 250 μm , 63 μm , 45 μm , 38 μm , 25 μm , and 20 μm openings. In order to process particles to eliminate large agglomerations

and large outlier or extraordinarily deformed particles, manually one must gently push particles through the sieve with the tip of their finger while wearing nitrile lab gloves and a respirator. Alternatively one can utilize an automatic process which includes passing the spheres through the sieves locked into a sieve shaker. This can be used equipped with a stack of sieves to even further select a specific range of spheres from the bulk of particles from the supplier. This method is time consuming and takes several hours to process several grams of spheres. It is also possible to incorporate a method known as wet sieving which uses a solvent with a lighter density than the particles to be sieved.

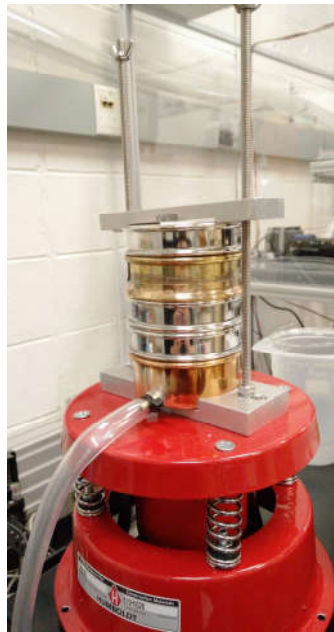


Figure 3.2: Humboldt Sieve shaker with several sieved secured on top of the spouted catching pan

3.4 Fluidization Mechanism

In order to ensure the most uniform coating of deposited material on to the spherical substrates, mixing or fluidization of the particles was a necessity. Several prototype mixing apparatuses were tested to understand the nature of the variously sized microsphere substrates. Early attempts to fluidize particles incorporated rolling dishes, piezoelectric transducers and audio speakers. The final method of fluidization includes a rotating particle dish mounted to an electromagnetic shaker that sits in a variable angled support bracket. The shaker is powered by a sinusoidal signal produced by an Agilent 33120A arbitrary waveform generator amplified by a Pyle 3100 Watts PQA3100 power amplifier. The signal is then measured off a BNC splitter attached to an electrical feedthrough located underneath the main chamber. The instrumentation required for measuring the shaker's input voltage is an Agilent 32201A Digit Multimeter. An upgraded gear motor assembly and rotary feed through the bottom of the chamber provide the rotation for the particle dish.

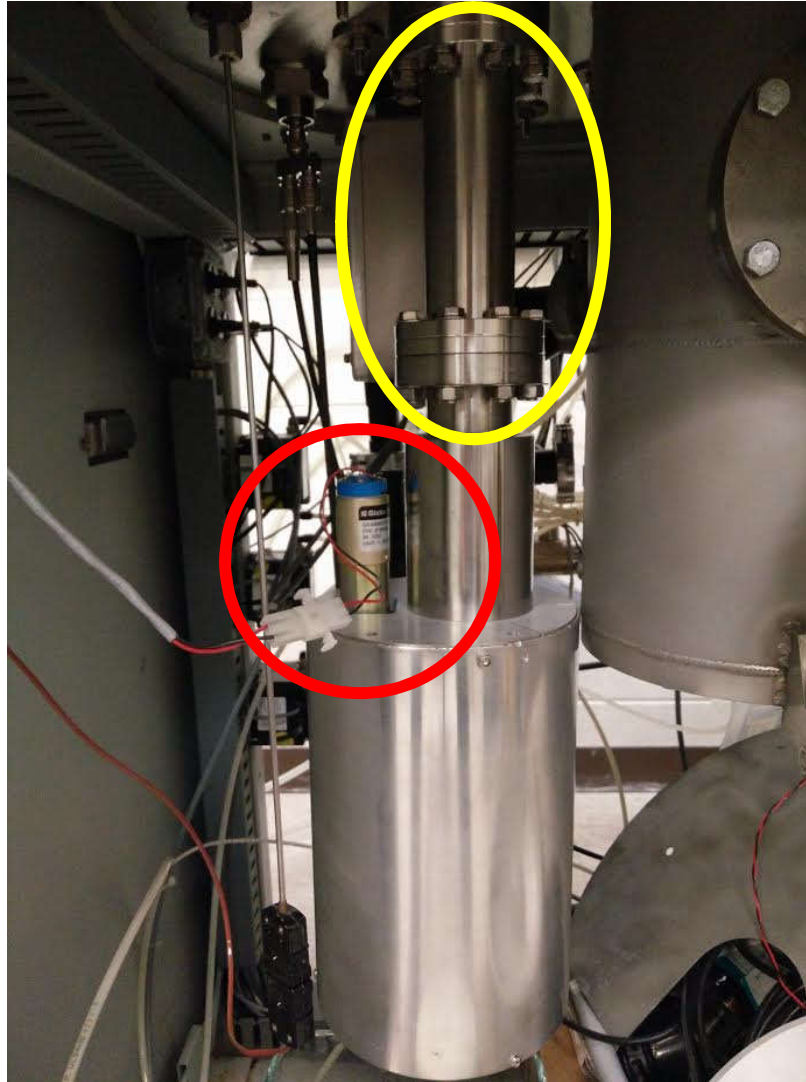


Figure 3.3: Gear motor and internal drive shaft assembly.

A faster gear motor with still an acceptable amount of torque was installed (circled in red) and an extension piece was added in order to lower the stage which originally protruded several inches from the baseplate into the chamber. This space was needed for the shaker assembly to fit properly within the path of the sputtered target material.

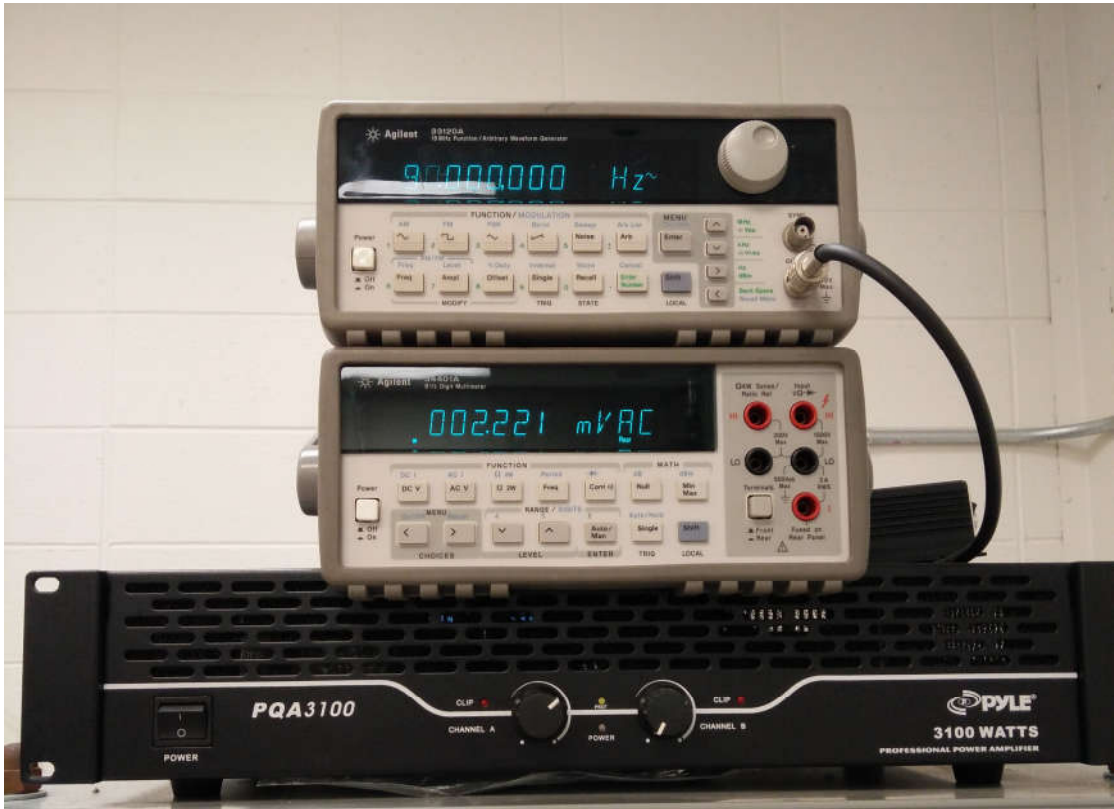


Figure 3.4: Instrumentation for generating and measuring voltage delivered to the electromagnetic shaker

The rotating particle dish and particle comb were designed in SolidWorks and was outsourced to ProtoLabs for fabrication. The particle dish features angled side walls that prevent particles from exiting the dish while allowing them to recirculate as it rotates. The particle comb is designed to be stationary while the particle dish rotates around it which acts to mix and break up particles and agglomerates. The rotation speed is adjusted by the control stack on the Denton sputter system and can reach about 4 rpm.

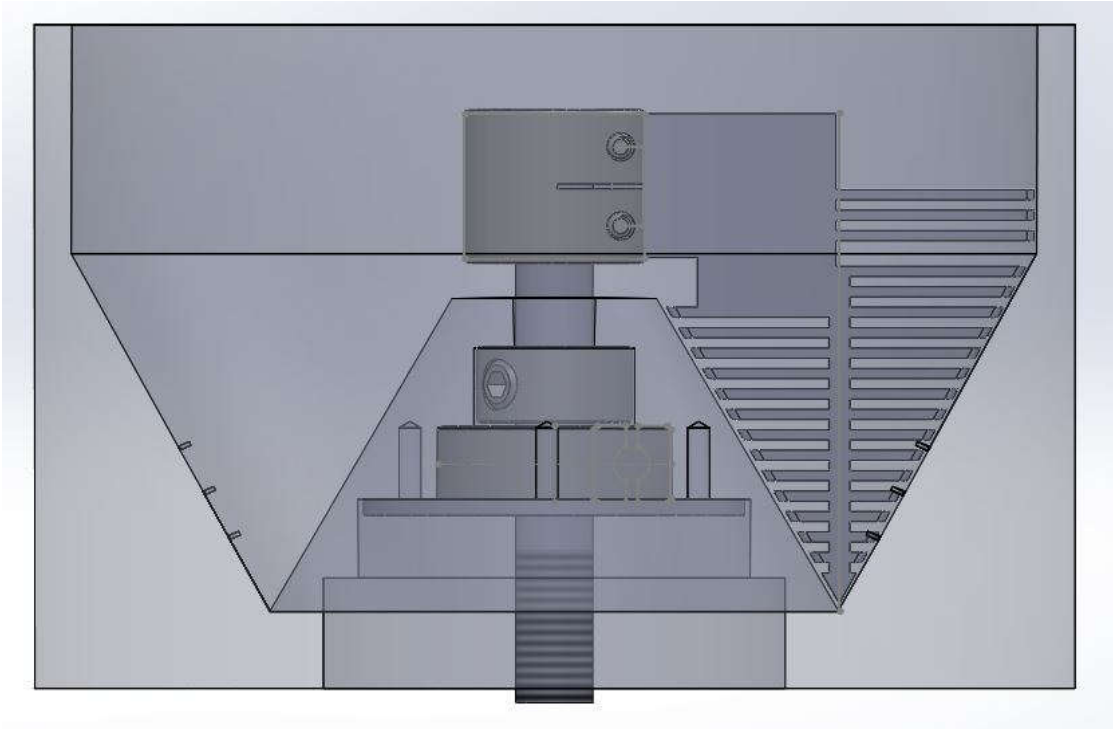


Figure 3.5: Side cross section view of final particle cup.

This final cup design is 5" in diameter by 3.25" tall. The hollow cavities seen on the center line are designed to hold an assembly comprised of a grease free bearing press fitted to a threaded rod in place by two rod collars on either side. On the top end of the rod is another collar with two through holes, which supports the particle comb.



Figure 3.6: Rod assembly

This rod assembly screws into the electromagnetic shaker and sufficiently translates the oscillating linear motion generated from the shaker to the particle cup thus, providing the agitation needed to initiate and sustain a fluidization of particles.

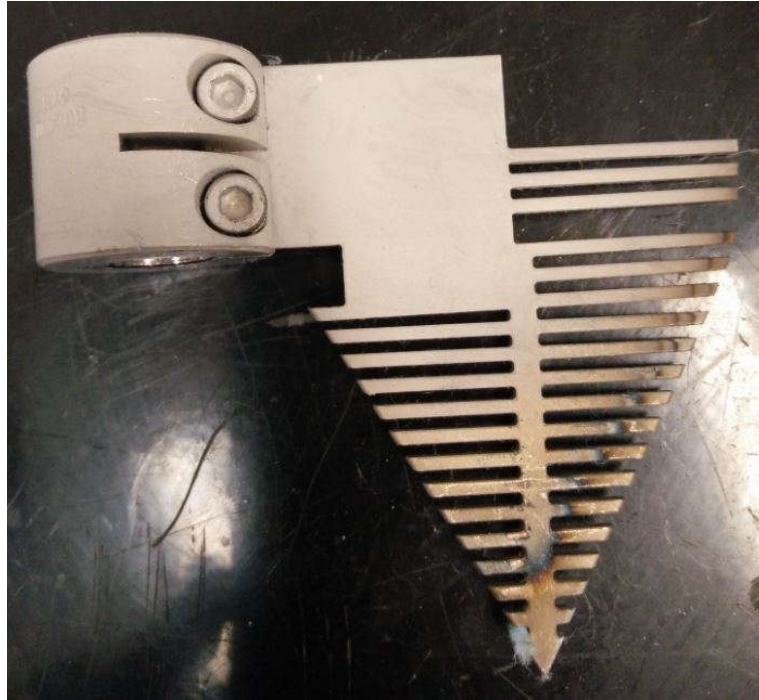


Figure 3.7: Particle comb and collar

The particle comb features teeth and teeth spacing of 0.05” this design proved to be suitable for allowing a reasonable flow of particles as they pass through due to the rotation of the cup and to gravity.

Particles of different average diameter and composition will behave differently to the means of fluidization. For example, the 20 μm uncoated HDPE microthene particles tend to clump more so than the SiO_2 microspheres, even after sieving through a 250 μm sieve to break apart large dense agglomerates. These HDPE particles were also the only ones, which seemingly, statically, stuck on to many of the utensils used for handling it, including the sieves, weigh boats, and glass containers. For the HDPE microthene an extra step was taken to sputter onto them. This special process is the

following. If the HDPE microthene spheres were to be deposited onto for more than four hours with Aluminum, they would first be sputtered for 4 hours with the particle comb raised about an inch or so. Having the comb raised this amount allows the mound of spheres to slide on the bottom of the particle cup as it rotates but also allows the bottom of the comb to scrape and knock the top of the mound of spheres over providing a mechanism for a normally non-ideal fluidization. After 4 hours of deposition with a non ideal fluidization, the HDPE microthene spheres have enough Aluminum coating that allows for the spheres to not clump as much and pass through the 0.05” teeth of the particle comb. For the remainder of the deposition time the comb is lowered and normal fluidization resumes.

3.5 Sputtering Process Parameters

Deposition experiments require special attention to several process parameters. Sputter specific parameters include vacuum pressure, process gas flow rate, deposition pressure, RF power, sputter time along with the angle of the shaker and particle cup and distance from the sputtering target. Parameters that change due to the mechanics of the fluidized particles include those related to the particle dish, namely shaker frequency and voltage.

Table 3.1: List of typical sputter parameters, values may change for special experiments or based on fluidization of particles

Parameter	Value
Cross over pressure	8.5E-2 Torr
Base pressure	1E-7 Torr
Sputter pressure	5E-3 Torr
Gas flow rate	20 SCCM
Plasma initiation @25W matching:	
CT	21.50 %
CL	93.20 %
Plasma sustaining @75W matching:	
CT	22.50 %
CL	65.90 %
Shaker driving frequency	90 Hz
Shaker driving voltage	9.5 V
Particle cup rotation	15 RPM
Particle cup angle	38°
Distance top of particle cup and target	3 in.

Chapter 4

CHARACTERIZATION

4.1 Materials Characterization Methods

In this chapter, I will discuss the means of characterizing layers deposited. The most valuable tool may have been the scanning electron microscope.

4.1.1 SEM Microscopy

Scanning electron microscopes (SEM) are a very useful tool of imaging when features are too small for optical microscopes. They are often combined with focused ion beams (FIB) and energy dispersive x-ray spectroscopes (EDS or EDX). The microscope utilized in throughout this thesis was a Zeiss Auriga 60 CrossBeam FIB/SEM located in the University's Keck Center for Advanced Microscopy and Microanalysis Interdisciplinary Science and Engineering Laboratory.

As the name suggests, an SEM detects reflected electrons from a sample that were emitted from a focused electron source that raster scans over the surface of that sample. The electron beam is focused from the gun by electro-optical lens elements located throughout the column [20]. Depending on how deep the emitted electrons penetrate the sample and how they are scattered back toward the detectors they will generate different qualities of data about the material composition. Secondary electrons (SE) provide surface topology information since these electrons do not penetrate deeply into the material due to their kinetic energy. Backscattered electrons (BE) provide more compositional based information as they possess the kinetic energy required to penetrate deep into the material. A unique detector captures each kind of scattered electron. Detectors were experimented with for imaging of the samples of this thesis and each produced images with mixed success. For most samples secondary

electron detection proved to be the most resourceful method of capturing quick and reliable images of microspheres and features deposited by sputtering. A clear example of each type of detector will be shown in a later section showing the visual differences of the images produced.

The preparation and process steps include; first placing a piece of carbon tape onto a sample stud, then dispensing a small amount of sample onto the carbon tape. The secured sample is then sputter coated for 60 seconds with Gold Palladium (AuPd). The AuPd and carbon tape provide a conductive matrix in order to mitigate charging effects during imaging. The sample holder is locked into loading chamber of the Auriga, position particular sample into the beams path, bring to a reasonable working distance, and focus image. If milling needs to be done then the sample holder is adjusted towards the FIB by finding the eucentric and coincident points, which is at a 54° angle towards the FIB.

4.1.2 EDS Analysis

Energy dispersive x-ray spectroscopy utilizes the interaction of incident electron beam with the molecular structure of a material to determine its elemental composition. Electron bombardment produces x-ray characteristic lines representing electron transitions between the inner electron shells of the material's constituent atoms. Since the total number of electrons occupying atomic shells with specific allowed energies characterizes each element, each will produce a unique x-ray line spectrum when bombarded with energized incident electrons. When a material is excited by an x-ray, an initial vacancy in an inner shell is generated. The transfer of an electron from another shell, which leaves behind a final vacancy, fills this initial vacancy. The energy of the line is the difference of the energies of the final and initial

vacancies. X-ray spectra lines are determined by the inner vacancy shell, common labels are K, L, and M. Lines are further identified by which group it belongs denoted by Greek lettering i.e. α , β etc., from most importance to least, and also by a number representing the intensity of the line within the group [22]. Energies are in units of keV. It is necessary to bombard the atoms with at least twice its critical excitation energy, which is dependent on the atomic number of the atom. In order to choose the correct energy to use in the Auriga SEM/EDS, the extra high tension (EHT) voltage level is adjusted accordingly. The following elements and their corresponding critical excitation energies were kept in mind when analyzing samples through EDS [21].

Table 4.1: List of useful critical excitation energies for EDS Analysis

Element	Critical Excitation Energy (keV)
Carbon	K α 0.277
Oxygen	K α 0.525
Aluminum	K α 1.486
Silicon	K α 1.739
Palladium	L α 2.838
Gold	L α 9.712 M 2.120

The Auriga SEM's ability to connect to EDS analysis software was utilized to characterize material composition of samples. It is possible through the Auriga 60 to perform different kinds of EDS scans. Precise line scans and mapping tools prove to be useful in determining levels of elements in a sample area by producing colorful, concise, graphs. It is suggested to perform EDS scans at around 8mm working distance on the Auriga 60.

4.2 Silicon on Silicon Dioxide Microspheres

This section will discuss the specific sets of microsphere that were focused on for developing effective fluidization, evaluating film quality and electromagnetic properties.

4.2.1 250 μm Silicon Dioxide Spheres

An early attempt to sputter Silicon on to spherical substrates utilizing a prototype particle dish was completed on to 250 μm solid SiO₂ microspheres.

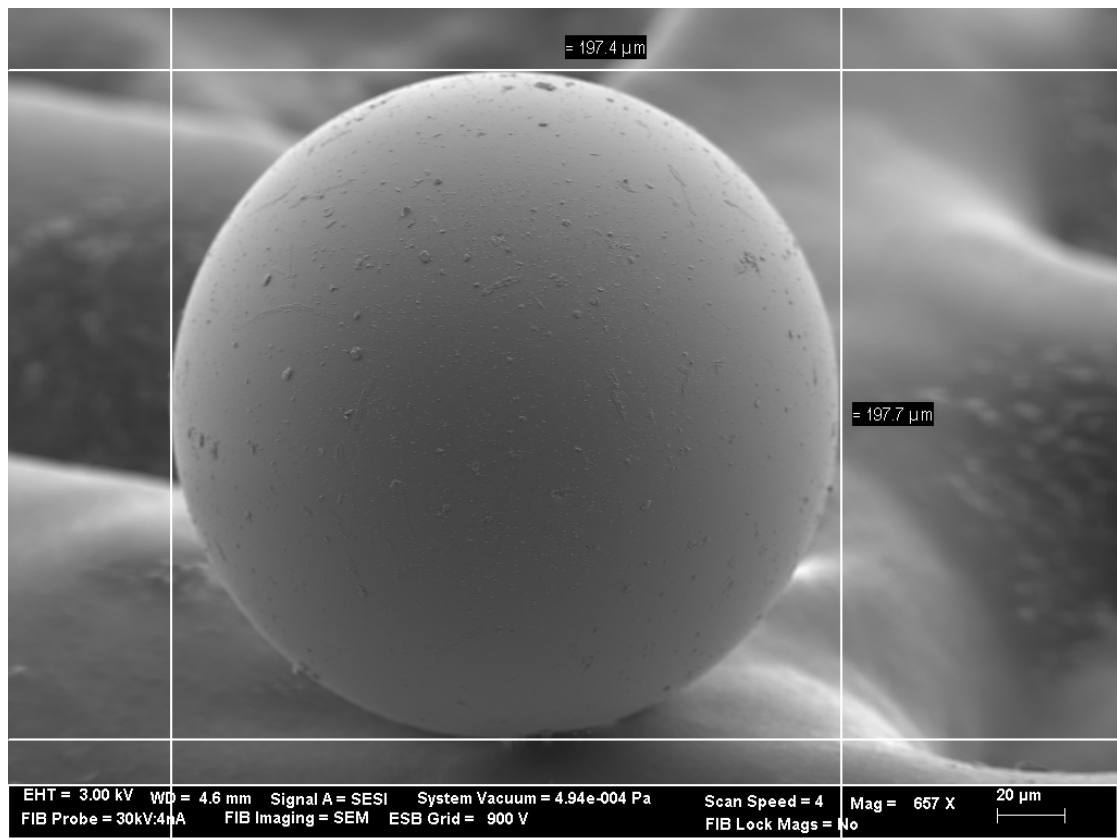


Figure 4.1: An uncoated 197 μm SiO₂ microsphere

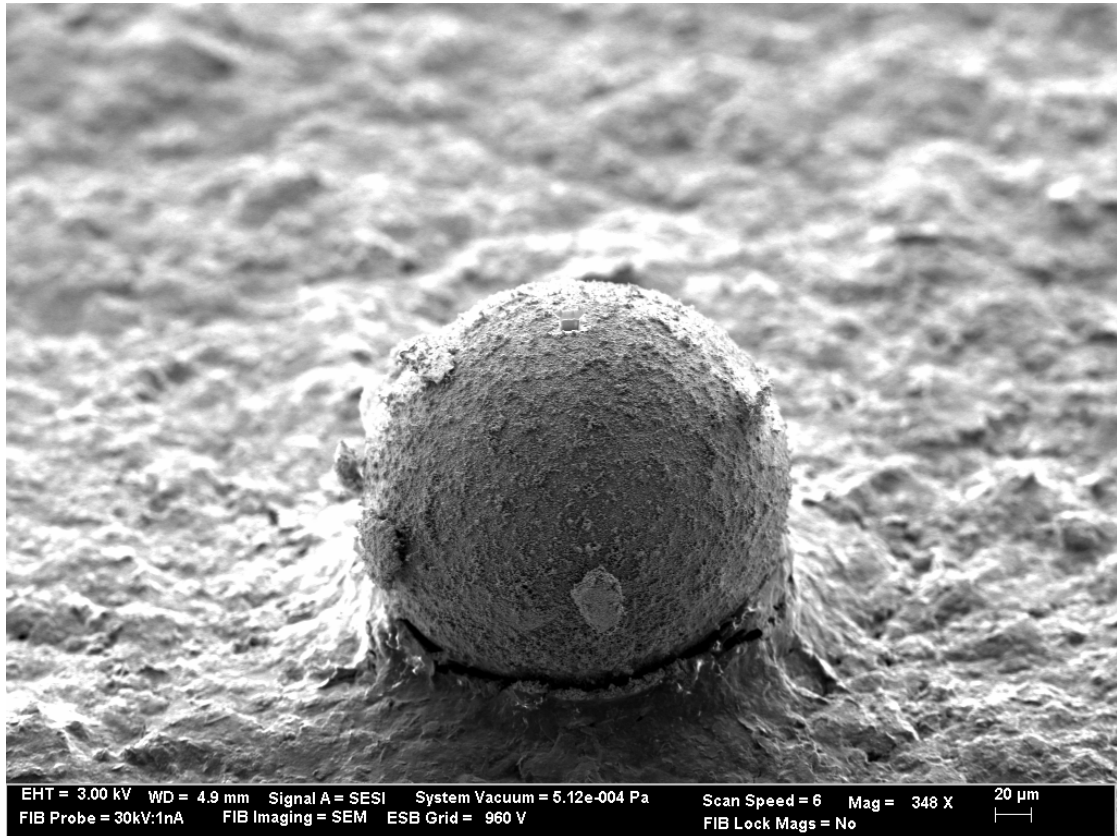


Figure 4.2: 26 hours of Silicon deposition on a 250 μm SiO₂ sphere

This sample was visually opaque before deposition and was almost completely black upon retrieval from the sputter chamber post deposition. Under SEM a thick and very rough layer is seen to be deposited onto the spheres.

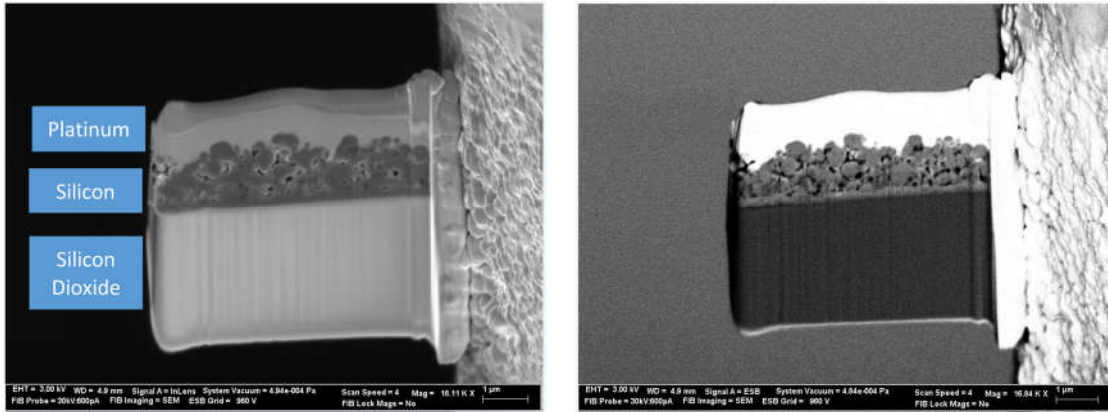


Figure 4.3: InLens (left) and ESB (right)

Utilizing two different detectors, a course layer of Silicon of about $1\mu\text{m}$ is clearly present on the surface of the SiO_2 sphere. This particular sample was also to be analyzed via transmission electron microscope (TEM) which was not able to produce any more meaningful results. The top layer of Platinum was deposited to protect the Silicon layer during milling and transporting on to the TEM copper grid on the right, which has the cross section welded to it.

This test on very large particles served as a proof of concept that encapsulating deposition may be possible though the method of sputtering on to a fluidized bed of spherical particles.

4.2.2 $2\mu\text{m}$ Silicon Dioxide Microspheres

Simulated design specification called for a $2\mu\text{m}$ base SiO_2 sphere with layers of alternating Silicon and SiO_2 . Efforts were made to fabricate this design by first depositing a layer of Silicon and characterizing it through SEM. At the scale of $2\mu\text{m}$ it becomes very difficult to first focus on the sphere itself and even more difficult to

narrow down any possibility of a deposited layer. Several SEM and TEM images were taken in attempt to find a silicon layer on a 2 μ m particle.

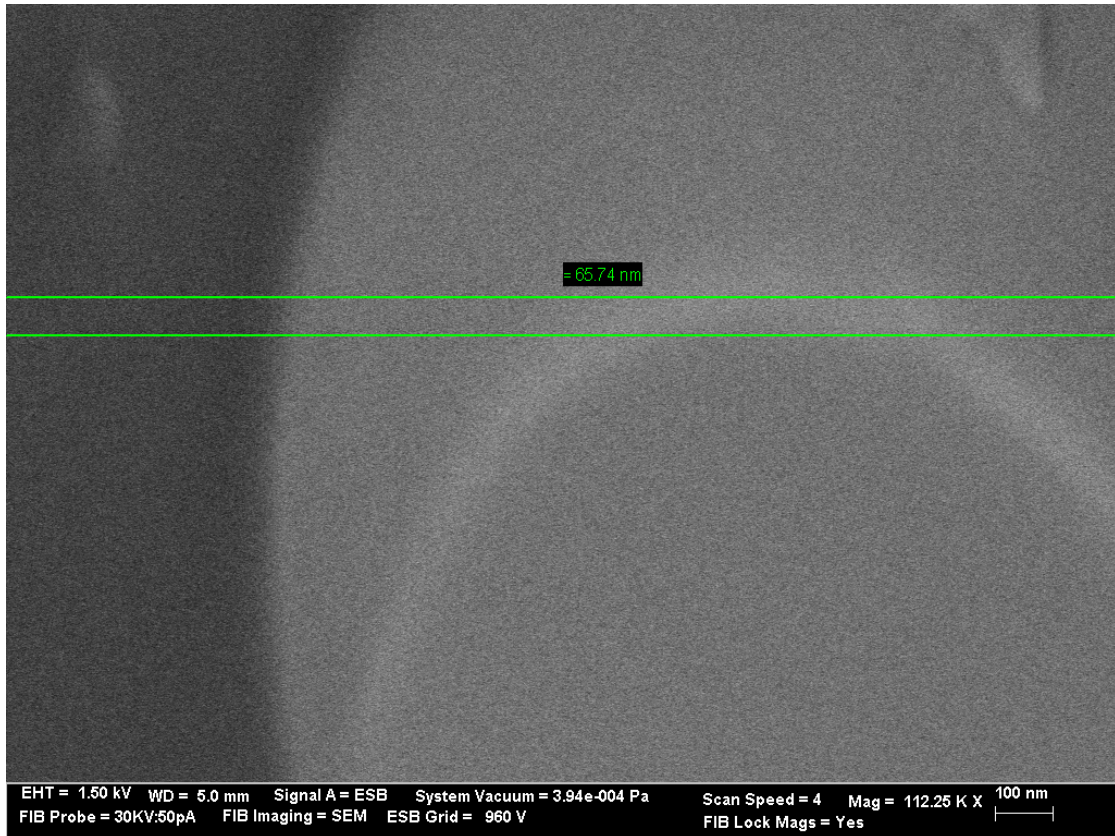


Figure 4.4: Silicon coated 2 μ m SiO₂ microsphere

The image above may show a distinction of a layer of Silicon but at this scale the limitations of the SEM does not allow the image to come into more focus to make a certain measurement. It was advised by the lead microscope scientist that this may be an edge effect and not a layer.

4.2.2.1 TEM Analysis of 2 μ m Spheres

A sample of 2 μ m silica spheres which were sputtered with Silicon for 7.5 hours were viewed by a transmission electron microscope (TEM).

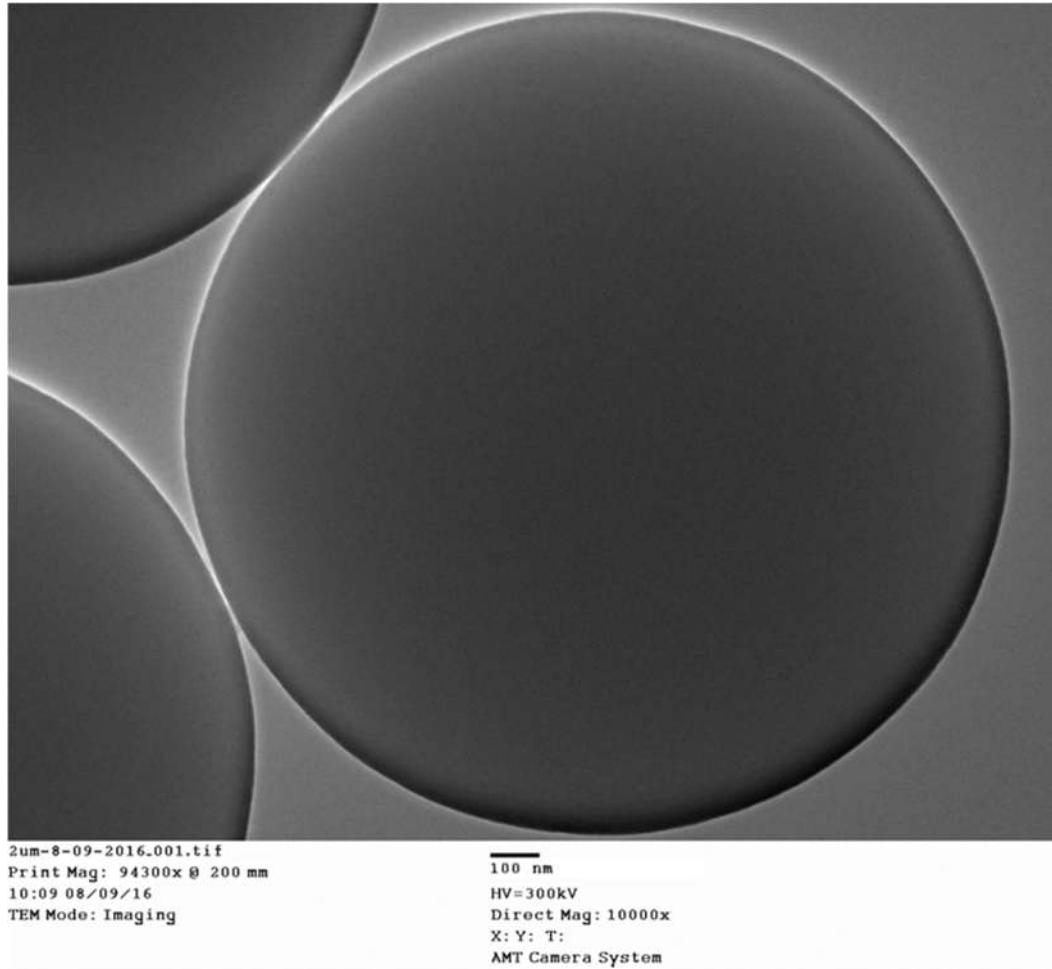


Figure 4.5: TEM of entire 2 μ m after 7.5 hours of Silicon deposition

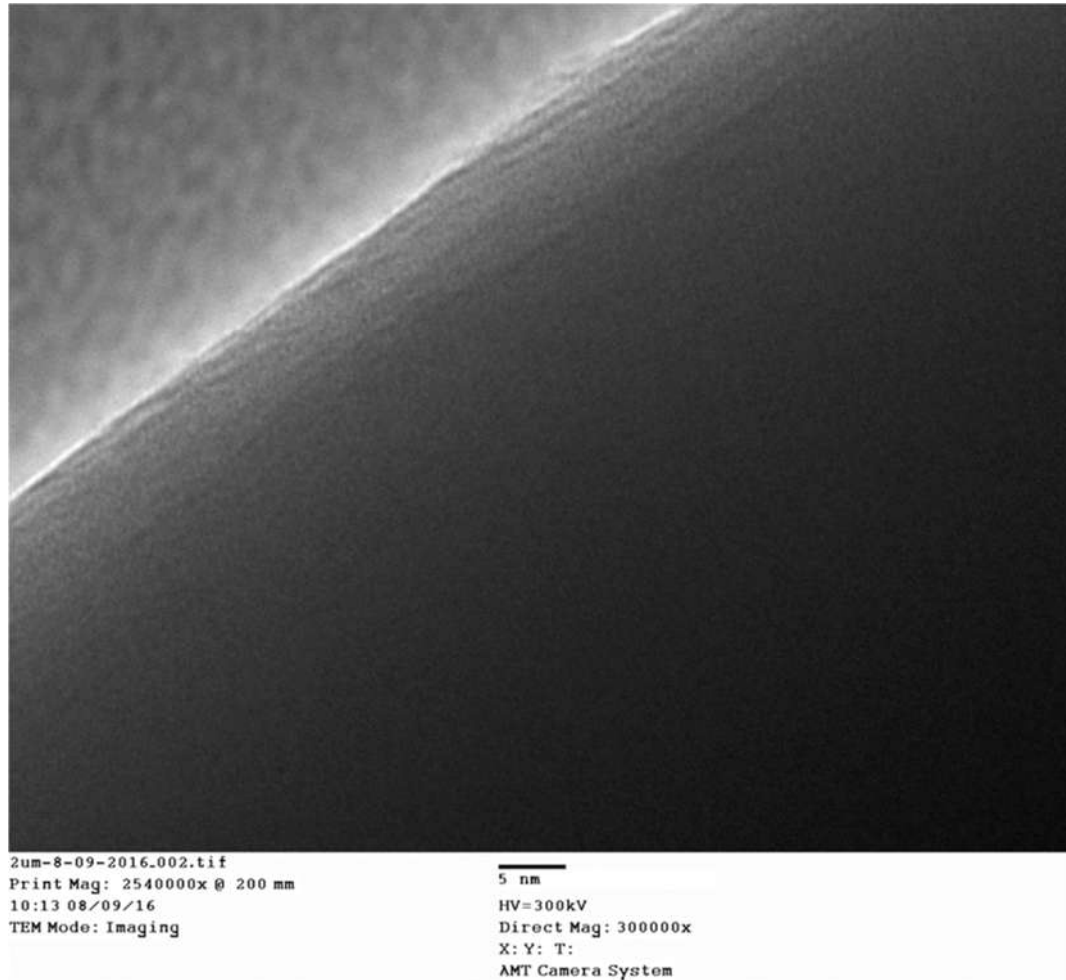


Figure 4.6: TEM of edge of 2µm after 7.5 hours of Silicon deposition

From the TEM images above, no conclusion can be made on the amount or existence of a Silicon layer on the sphere.

4.2.2.2 Mixing in 40µm Spheres into 2µm Spheres

Another study was done to observe the effects of incorporating larger 40µm spheres into a sample of 2µm spheres. The intention of this experiment was to better break apart agglomerates of 2µm particles with the help of the heavier 40µm particles.

Granular convection predicts that larger objects will eventually make their way to top. During fluidization, it was observed that this was true and that the overall bed did seem to mix somewhat more efficiently than if the entire bed was only containing $2\mu\text{m}$ spheres. SEM images were taken of the results.

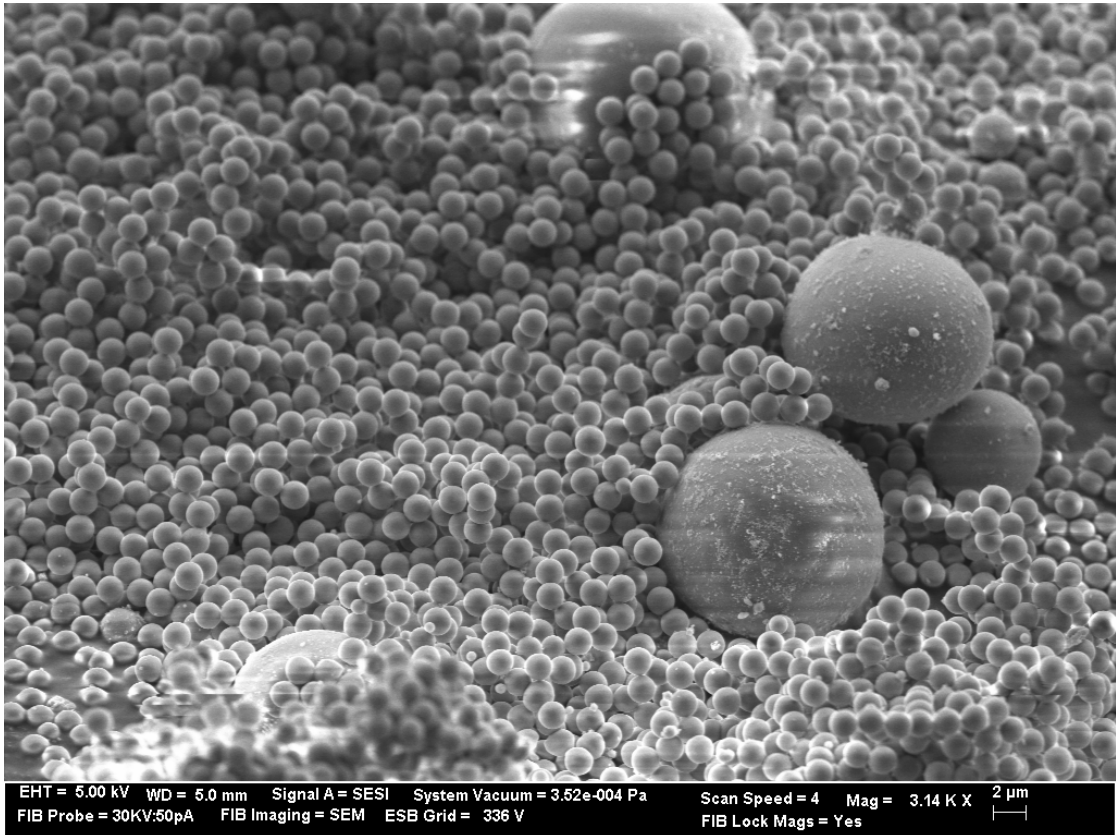


Figure 4.7: 1.25g of $40\mu\text{m}$ spheres mixed into 3.75g of $2\mu\text{m}$ sputtered with Silicon for 4 hours

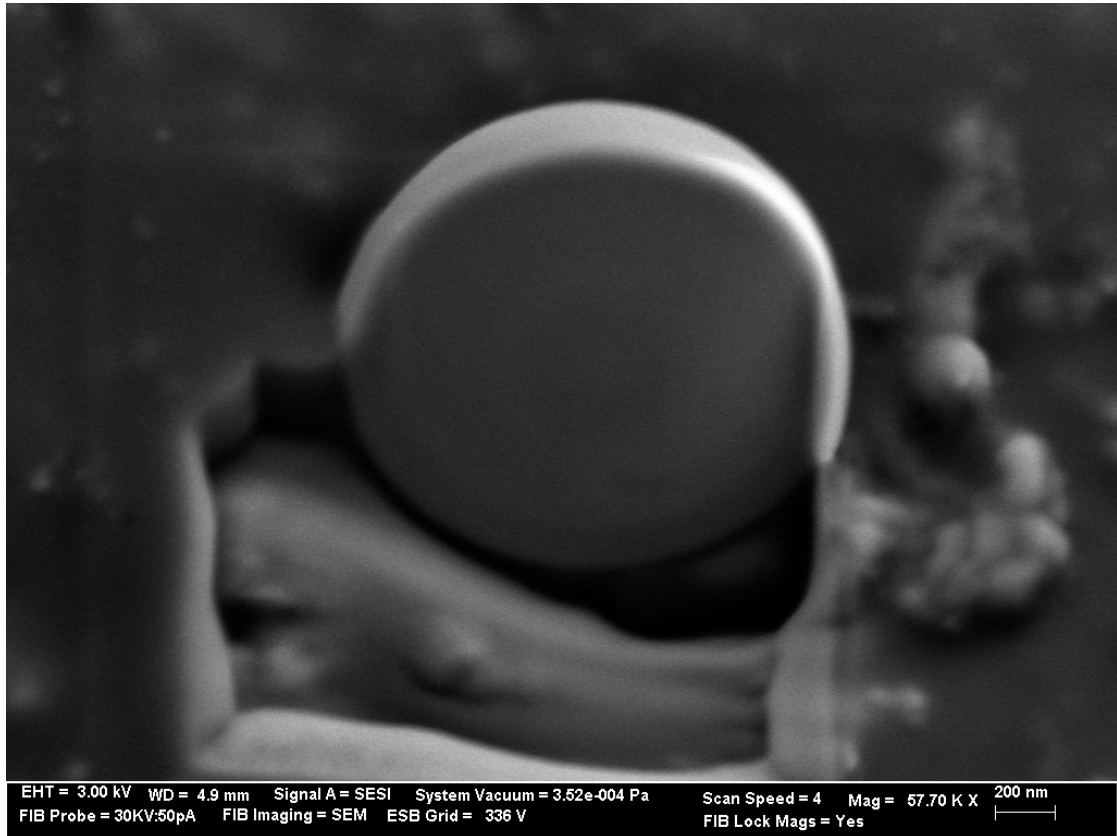


Figure 4.8: Cross section of a 2 μ m sphere from mix

In this SEM image utilizing SESI detection it can be seen that the sphere has been heavily damaged by the focused ion beam used to mill it to a cross sectional view. The top has been deformed and any layer of Silicon has probably been milled away. The bottom half of the sphere is less affected by the FIB. However, there are no detectable signs of a Silicon layer.

Unfortunately, even though visually the 2 μ m sample sets were altered, post deposition the samples sets were much darker, microscopy was not able to discern a layer thickness.

4.3 Planar Deposition Rate

With the new Cryopump and VAT valve additions to the sputter system, some planar depositions were completed to estimate depositions rates. A 500 μm thick, n type, 100 oriented, silicon wafer was used as the substrate. First Aluminum was sputtered onto the substrate for two hours. Two hours of Silicon sputter deposition followed.

The depositions were completed with the standard 20 SCCM of Argon gas flow kept at a pressure of 5 mTorr. The RF power used was 75W. The Substrate was placed on a planar rotating platform to reduce effects of uneven sputter gradients.

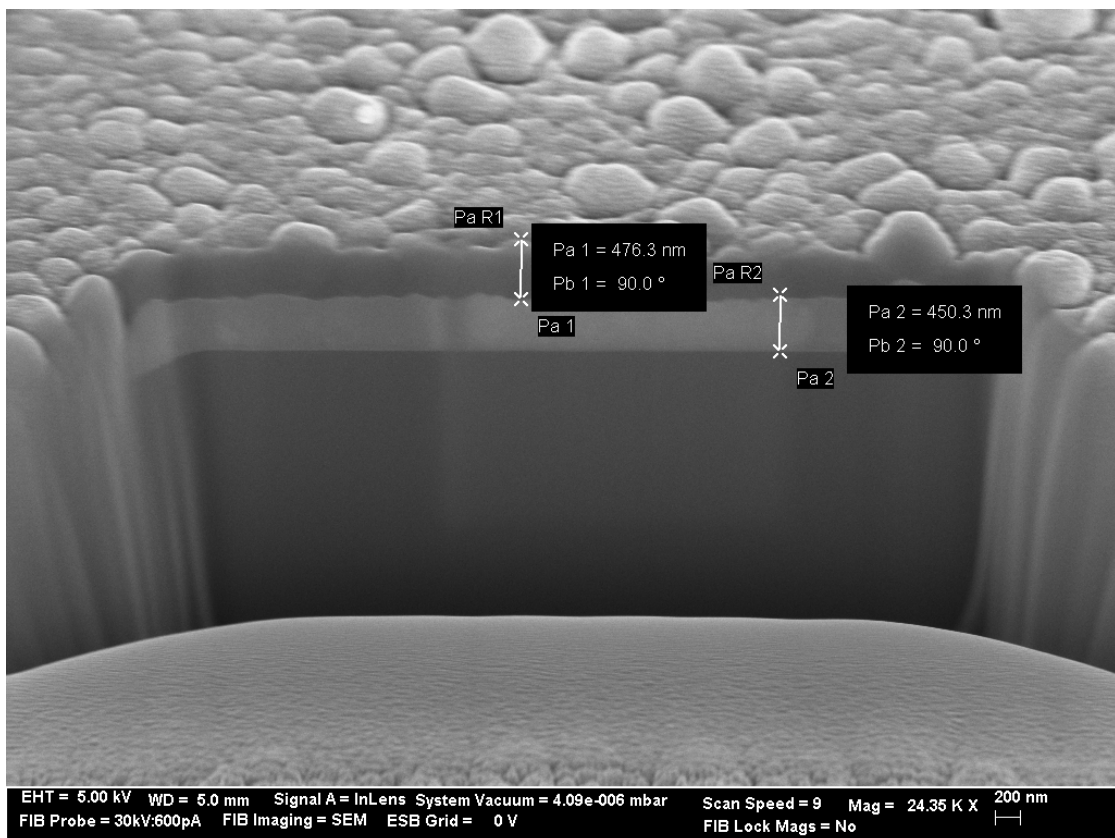


Figure 4.9: Planar deposition for rate estimation

After two hours of sputtering Aluminum there was a result of about 450.3nm which would yield 225.15nm per hour. After another two hours of sputtering Silicon there was a result of about 476.3nm, which yields 238.15nm per hour.

With this rate, it would take approximately 15 hours to deposit 5nm of uniform coating onto 5 grams of all 11 μ m wide spheres, this takes in account a packing factor of 0.64 and a top sputter area of about 25cm². The large amount of time for such a small thickness is due to the extremely large surface area of all of the spheres in a sample. There can be upwards of billions of spheres in a 5g sample resulting in a total surface area of up to 2m².

4.4 Aluminum Study

Several samples were fabricated, characterized via SEM techniques and sent to nanoComposix for electromagnetic analysis verification. The samples were the following:

Table 4.2: Sample description of six samples prepared for nanoComposix analysis

Sample #	Substrate Material	Average Initial Diameter (μ m)	Hours of Aluminum Deposition
1	Hollow SiO ₂	9-13	0
2	Hollow SiO ₂	9-13	8
3	Hollow SiO ₂	9-13	24
4	HDPE	20	0
5*	HDPE	20	4
5**	HDPE	20	8
6	HDPE	20	24

* Sample analyzed only through scanning electron microscope

** Sample analyzed only through mass extinction coefficient

4.4.1 Sample Preparation Process and Fabrication Parameters

The seven samples were fabricated in similar fashions of first pre-sieving, with 20 μ m sieve for the glass, and 25 μ m sieve for the HDPE samples. Samples of 5 grams mass were then measured and placed in to the fluidization bed, particle cup. Optimal fluidization parameters such as shaker voltage amplitude and frequency and particle cup angle were then manually adjusted and documented. The hollow SiO₂ sample was fluidized at 15.48V and 90Hz, while the HDPE sample was fluidized at a shaker voltage of 9.5V and frequency of 90Hz. The SiO₂ microsphere sample was fabricated over three days of 8 hour depositions. After the first and the final depositions, small samples were retrieved for SEM and mass extinction characterization. The HDPE sample was fabricated over four days of deposition. The first day's deposition lasted for 4 hours with the particle comb partially lowered. This was done to prime the HDPE microspheres with a small amount of Aluminum so that they would then freely flow through the spacing between the teeth of the particle comb, otherwise free flow fluidization was not achievable, a small sample was retrieved which would later be used for SEM imaging. This priming step was not necessary for the SiO₂ microspheres. The next day the comb was lowered and deposition lasted for 8 hours, a small sample was retrieved which would later be sent to nanoComposix for mass extinction analysis. The next two days were 4 hour and 8 hour depositions to result in a total of 24 hours which small samples were retrieved for both SEM and mass extinction characterization.

4.4.2 SEM Imaging

SEM images were collected of the samples prior to shipment to nanoComposix.

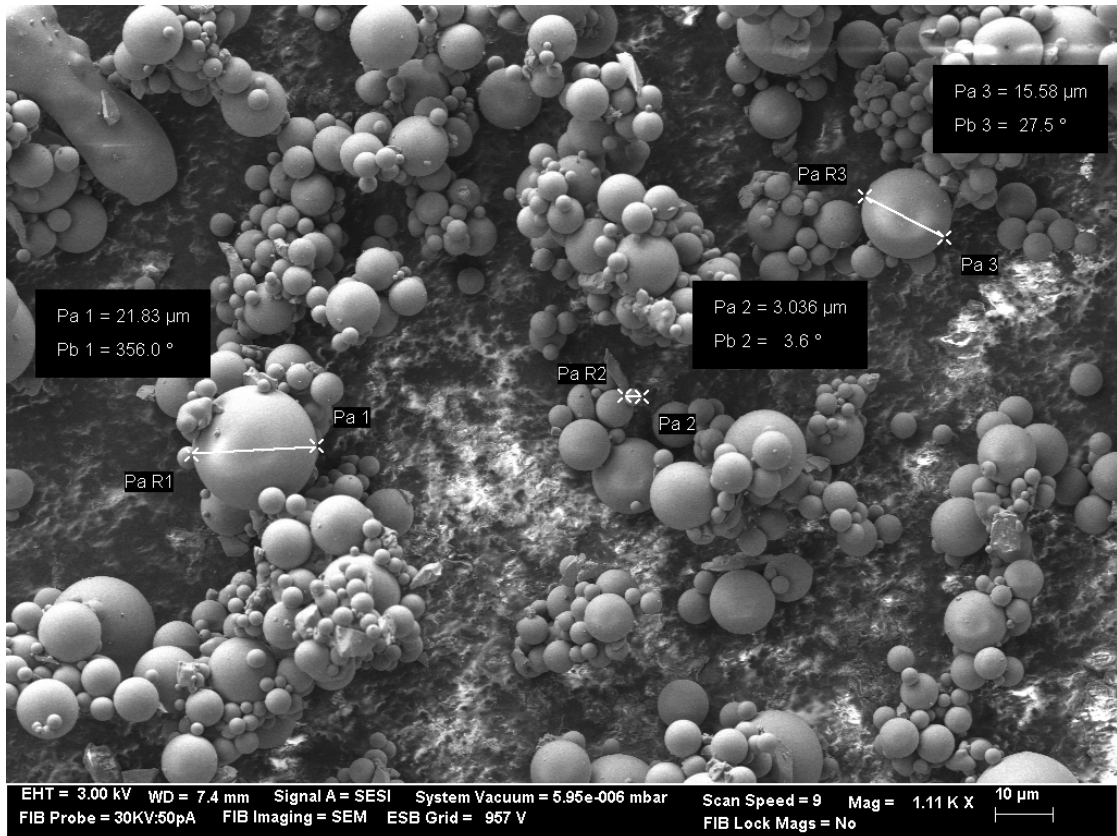


Figure 4.10: Uncoated hollow glass microspheres.

The above figure shows the great range in size of particles. The expected average diameter of these hollow glass spheres was reported by the manufacturer to be between 9μm and 13μm, however particles as small as a couple microns to as large as about 20μm. Even though the SiO₂ sample was passed through a sieve with 20μm openings, there are still a few particles that are slightly larger.

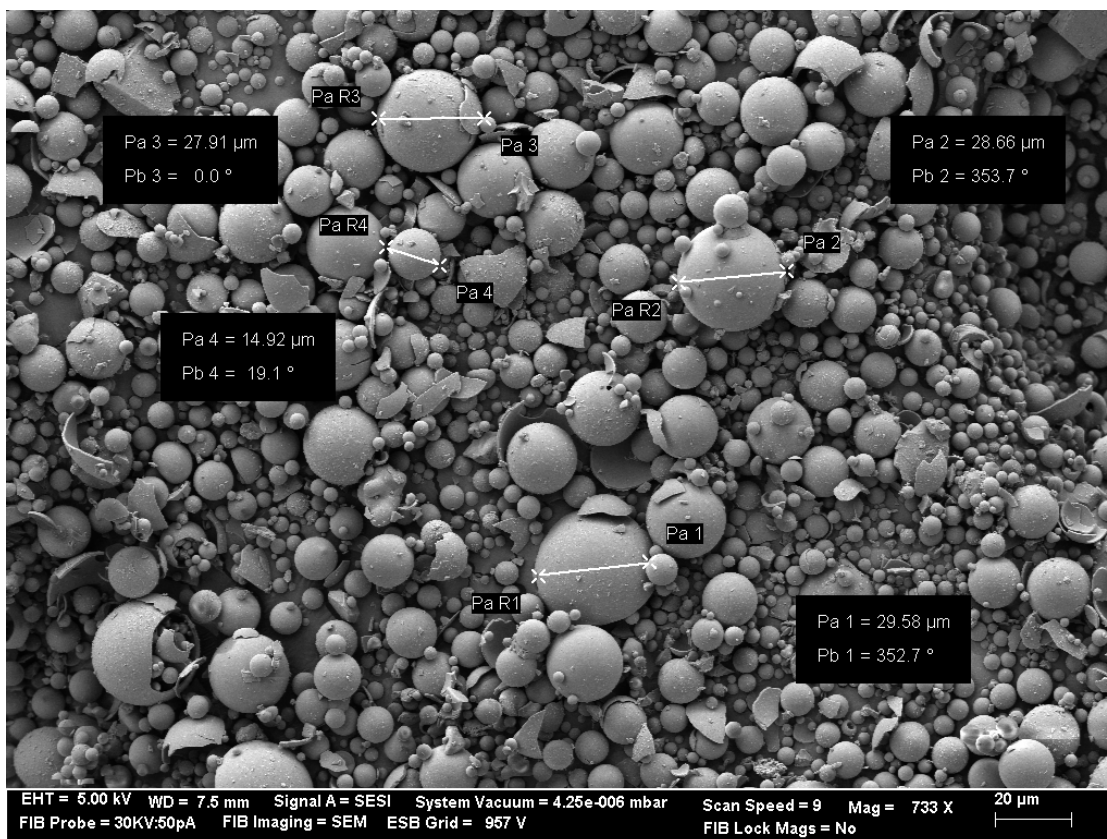


Figure 4.11: 8 hours of Aluminum deposition on several hollow SiO₂ spheres

After 8 hours of Aluminum deposition, a light dusting of material becomes observable, as seen on the next sample shown in the figure above. Broken shells are also present; this is most likely due to the harsh physical means of fluidization during the deposition process. It may be possible to sieve a fraction of the miscellaneous particles, post deposition, to attempt to create a better uniform sample, which in turn would produce a more regulated mass extinction infrared spectrum response.

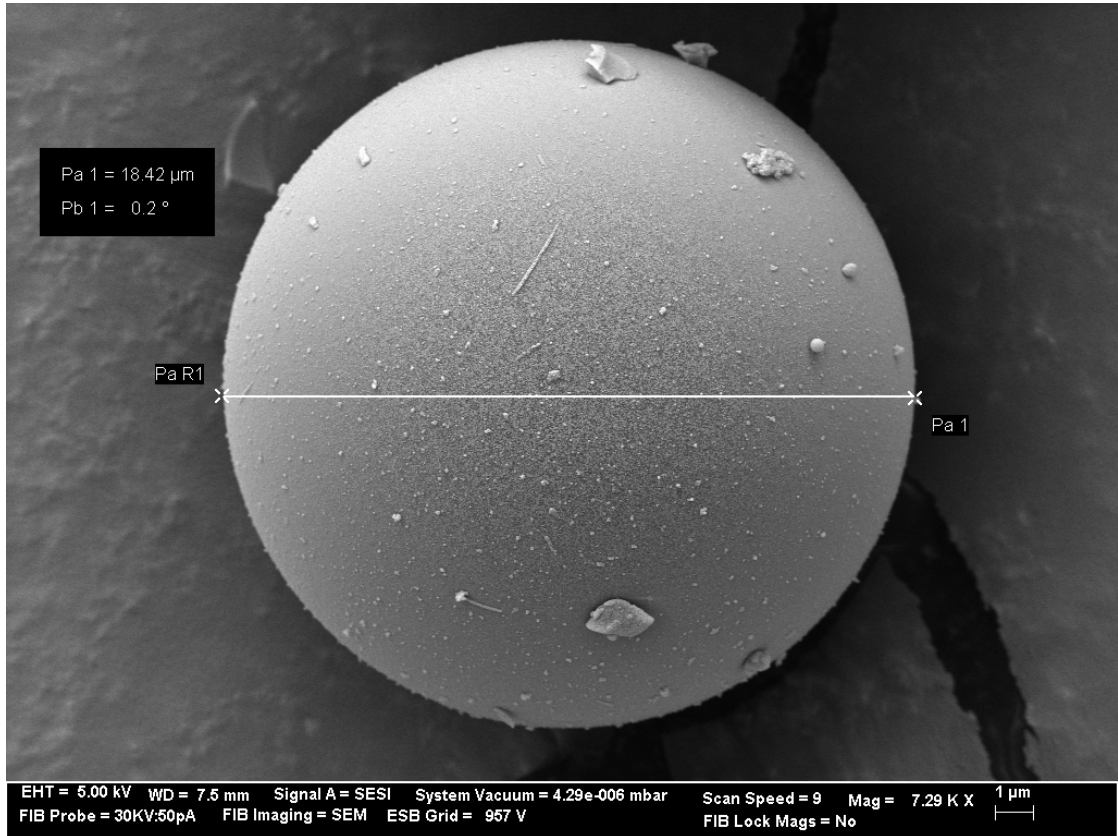


Figure 4.12: 8 hours of Aluminum deposition on a larger hollow SiO₂ microsphere

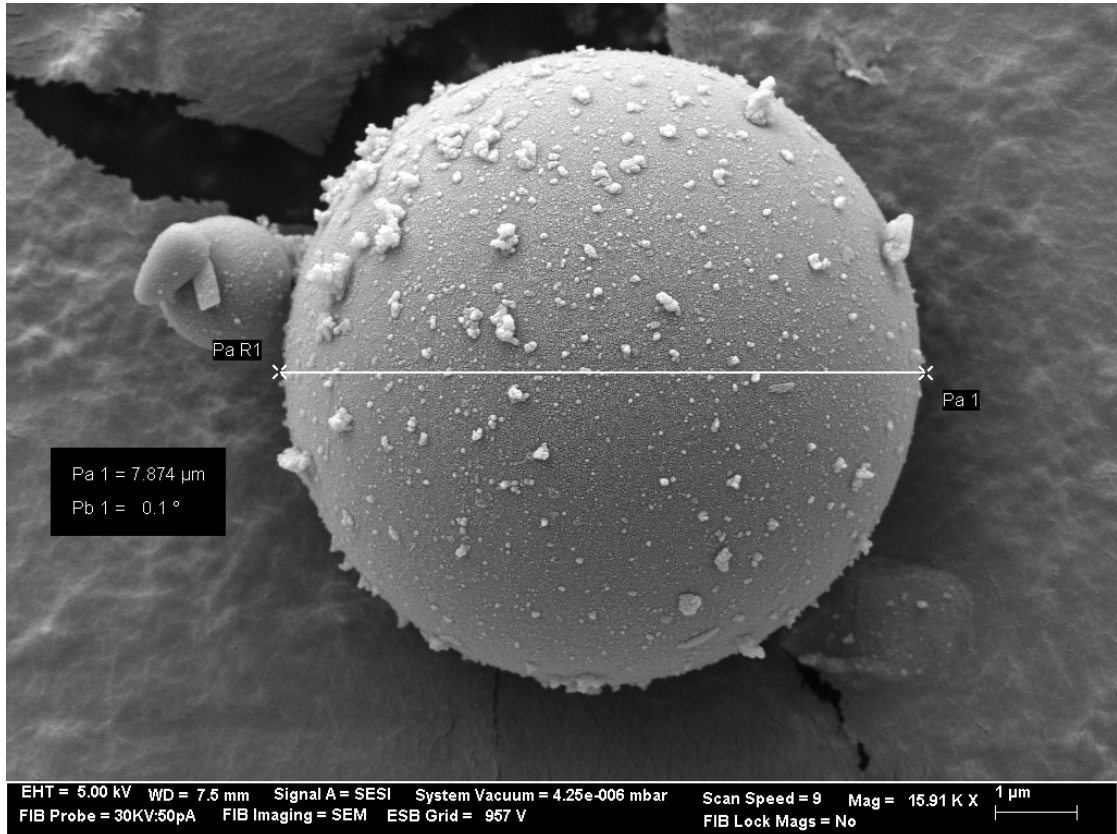


Figure 4.13: 8 hours of Aluminum deposition on a smaller hollow SiO₂ microsphere

The two figures above show two particles just outside the average diameter. The first being larger at 18μm, and the second being nearly 8μm. Also, it can be seen that each holds a different amount of added material to the surface with varying covering densities. From these views it can be noted that the deposited layers do not seem to be uniform by any stretch of the imagination. However, it is a good sign that Aluminum deposition is possible.

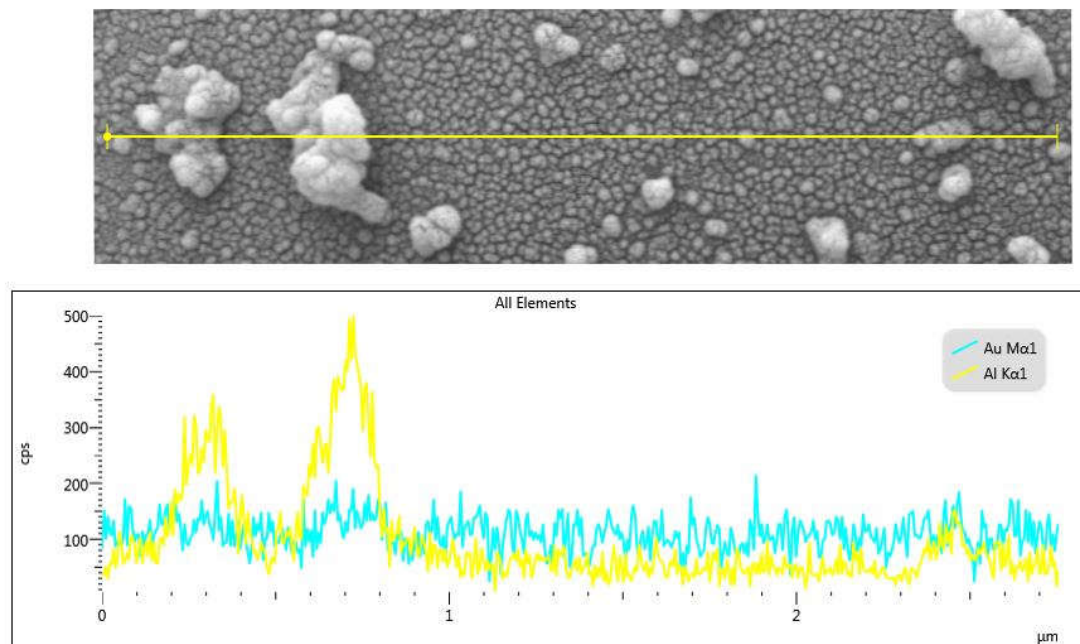


Figure 4.14: EDS line scan of 8 hour Aluminum deposition on hollow SiO₂ microsphere surface

An EDS line scan was done at an EHT value of 5kV, in order to efficiently discern traces of Aluminum and Silicon, and at a working distance of 7.5mm. This line scan reveals that the large rocky formations on the surface are comprised of Aluminum. These EDS parameters were also able to sense that the smaller pebble like features may be the monolayer of AuPd.

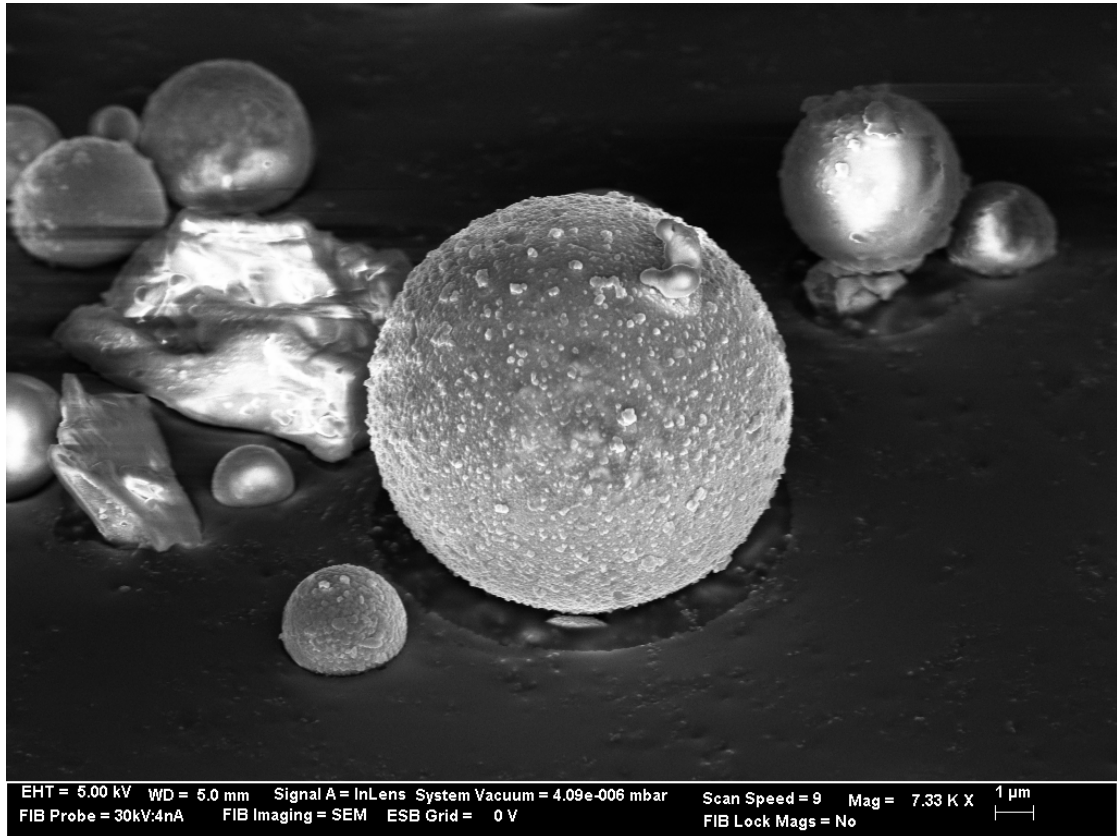


Figure 4.15: Surface morphology of 24 hour Aluminum coating on hollow glass microsphere

Aluminum deposition lasting of 24 hours produced coatings with high surface roughness as seen in the figure above on the main sphere. The diameter of which is roughly $10\mu\text{m}$.

In this image it is possible to notice the effects of the FIB gun while on but not milling. Underneath the sphere, a shadow effect is visible. In the shadow area the material is not milled by the imaging FIB, however the area exposed are being slightly eroded. This will be a challenge when imaging finer features.

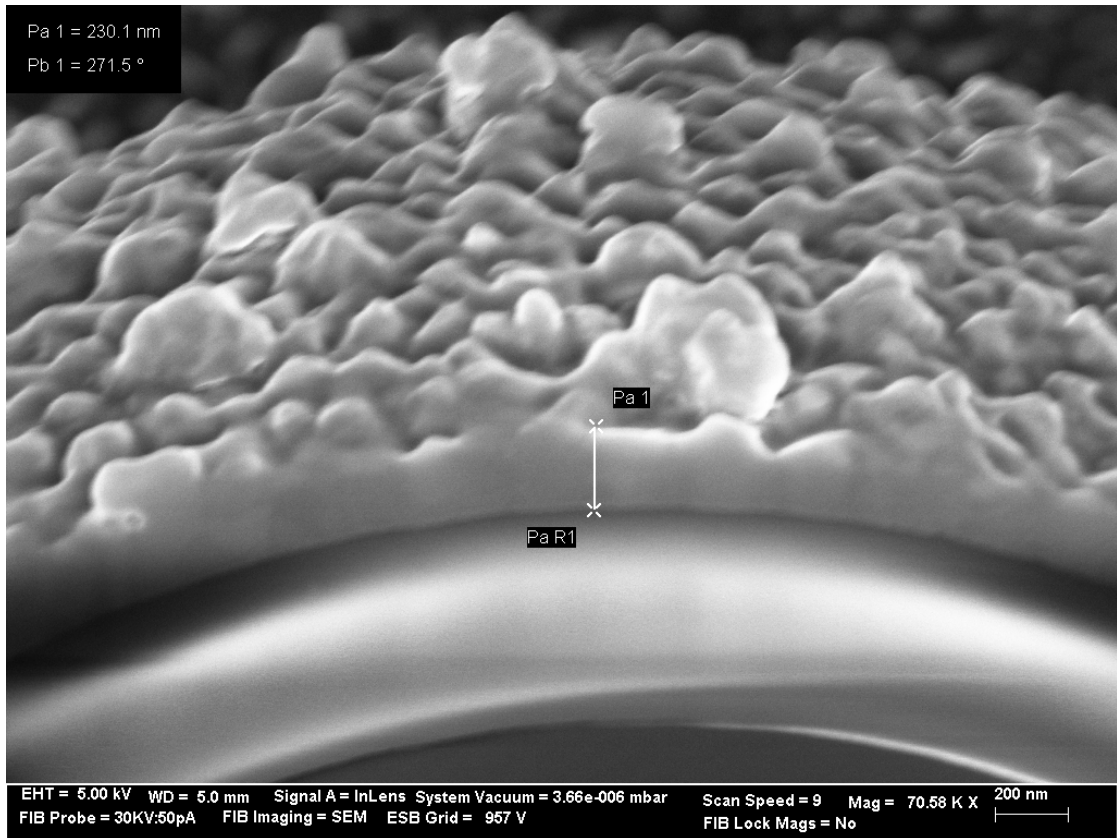


Figure 4.16: Cross sectional view of a 24 hour Aluminum coated hollow SiO₂ microsphere via InLens detection

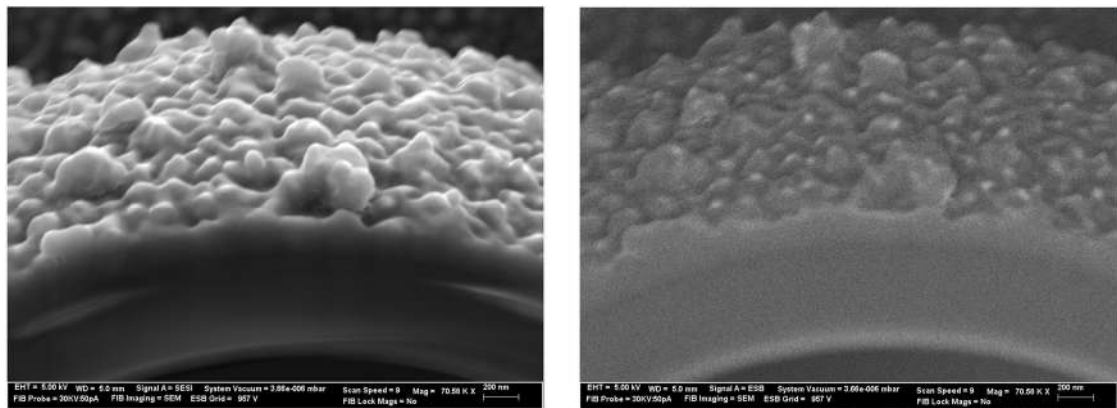


Figure 4.17: Cross sectional view via SE-SI (left) and ESB (right) detection methods

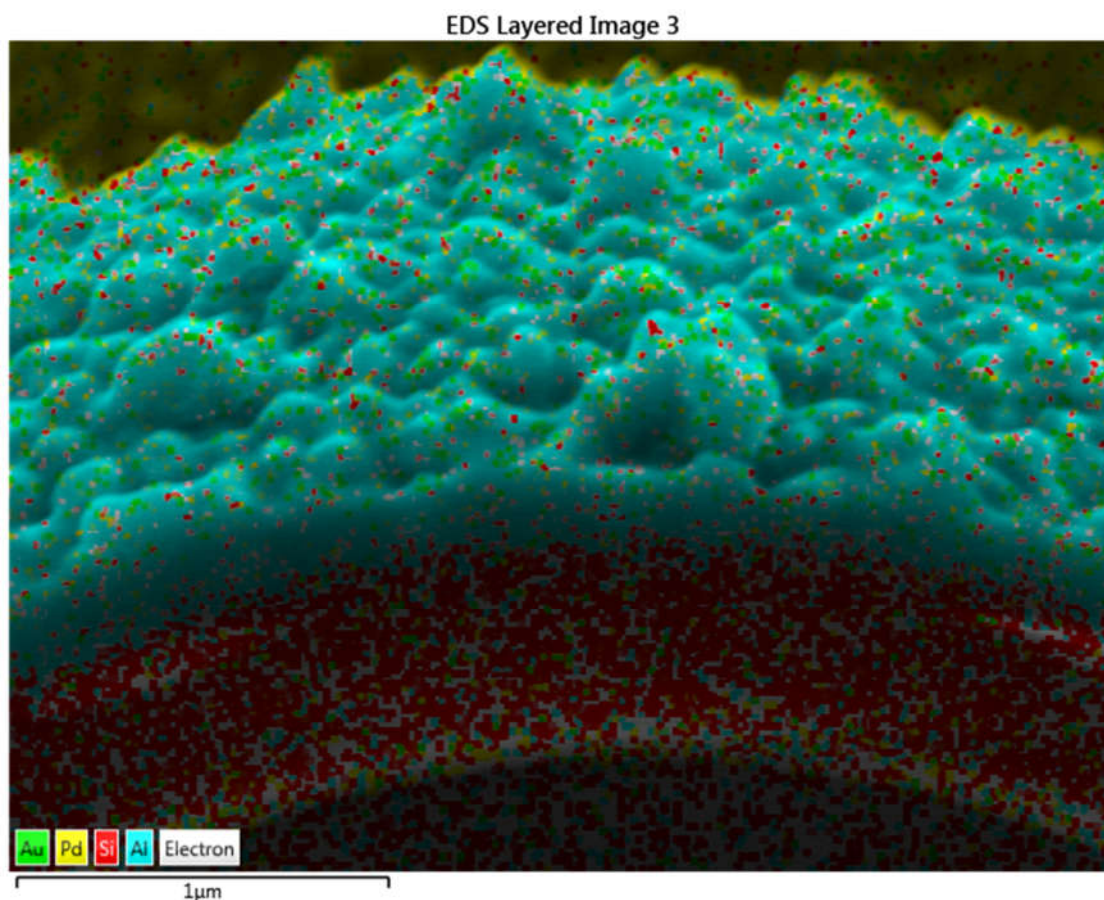


Figure 4.18: EDS Image of 24 hour Aluminum coated hollow SiO₂ microsphere

A cross sectional viewed image was taken of this sphere by milling half of it away by the Auriga's focused ion beam. Three of the microscope's detectors were used to visually compare their effectiveness in discerning potential layers. The detector that proved to provide the clearest image in this instance was the InLens detector. Both the SESI, which captures secondary scattered electrons, and the ESB, which captures back scattered electrons were able to detect the layer with slightly less precision or visual clarity.

A 3D mapping by EDS was also completed on the image. The results of the EDS show that the layer perceived in the SEM images is in fact Aluminum. Silicon was discovered within in the substrate and Gold-Palladium was discovered on the surface, which was expected.

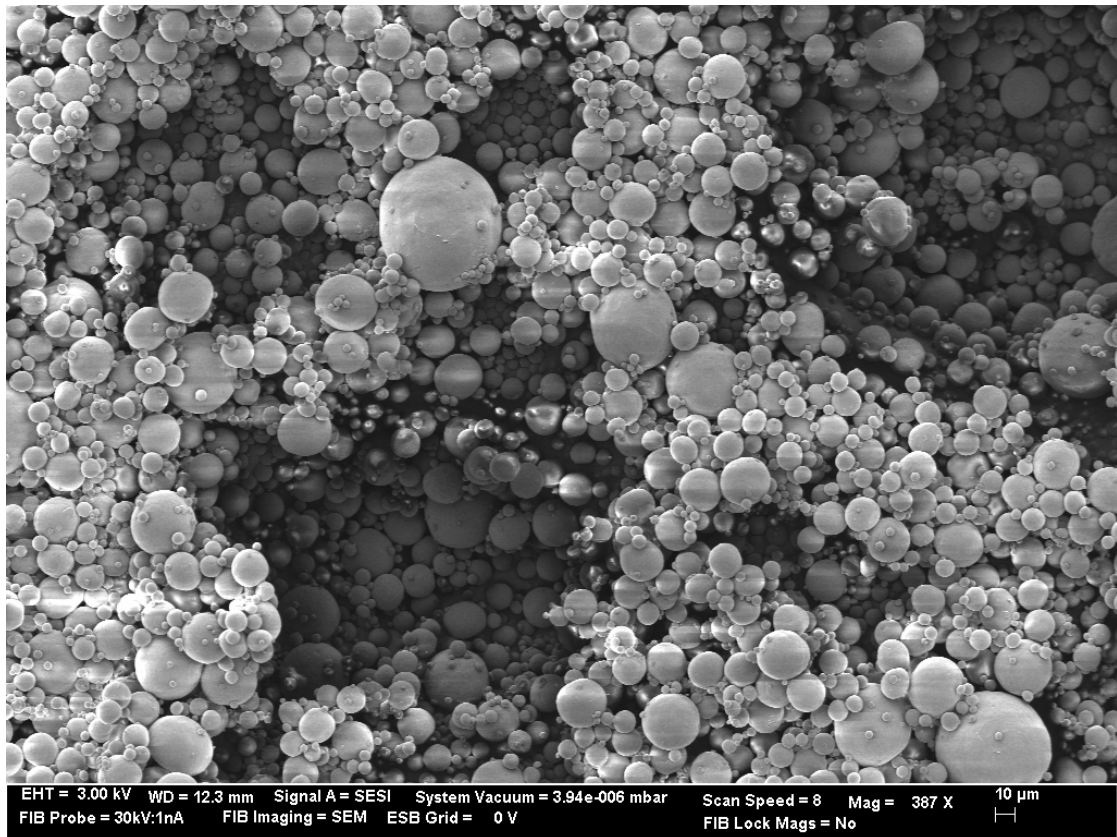


Figure 4.19: Uncoated HDPE

Initial SEM imaging of the uncoated HDPE microthene spheres reveal that they are highly polydispersed and less spherical in geometry compared to the glass microspheres.

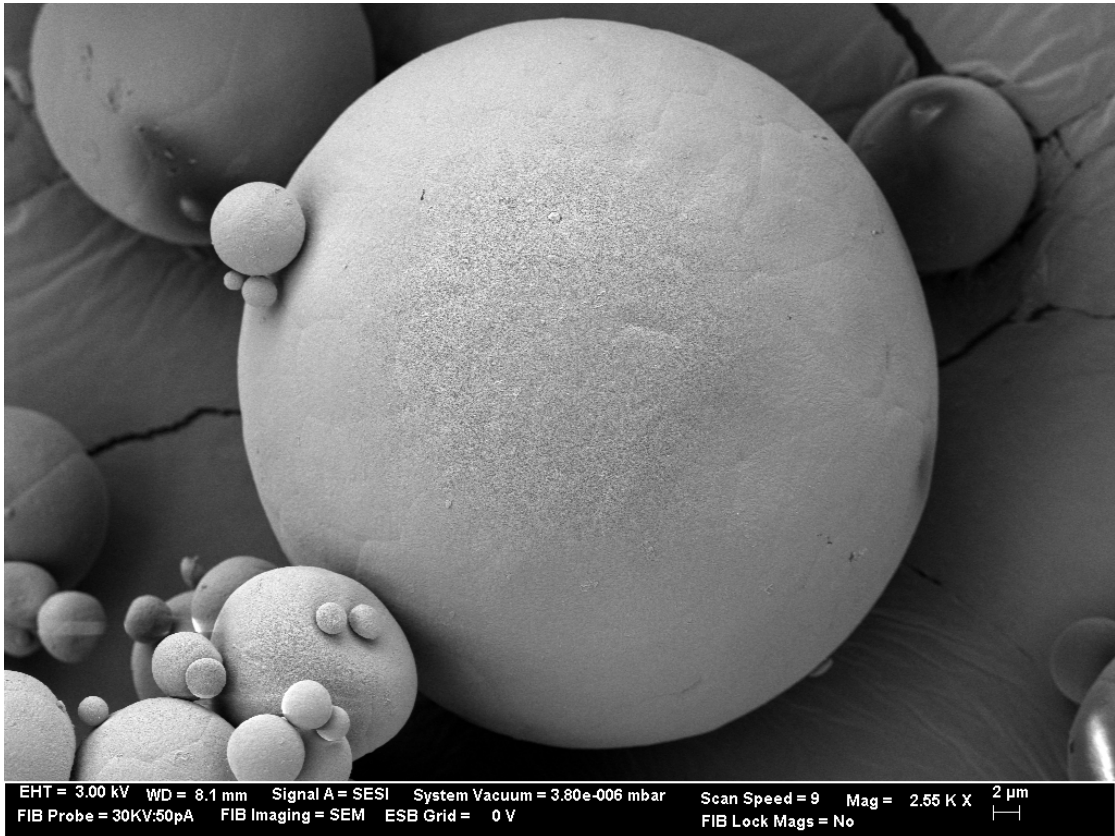


Figure 4.20: 4 hour aluminum on HDPE

SEM imaging of this 4 hour Aluminum coated HDPE sphere shows a rougher surface texture that was not present on the uncoated samples, indicating successful adhesion of Aluminum onto the surface.

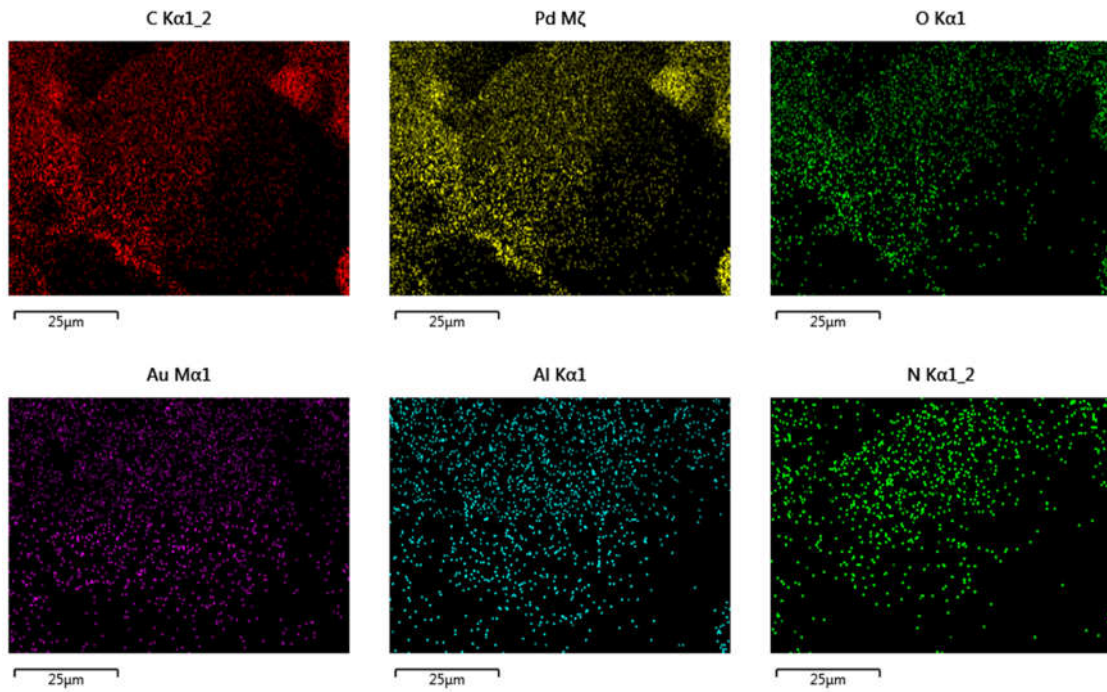


Figure 4.21: EDS mapping of 4 hour Aluminum deposition on a HDPE microsphere

An EDS analysis was taken to verify the material of the sample, an EHT of 3kV and working distance (WD) of 8.1mm was set. Carbon is found through the sample due to the carbon tape and composition of the HDPE polymer. AuPd is also found everywhere since an AuPd coating is done prior to imaging. There is a small concentration of Aluminum outlining the sphere which may indicate some aluminum on the surface, however it isn't at a high enough contrast to warrant reason to believe there is a thick layer, just that Aluminum is present.

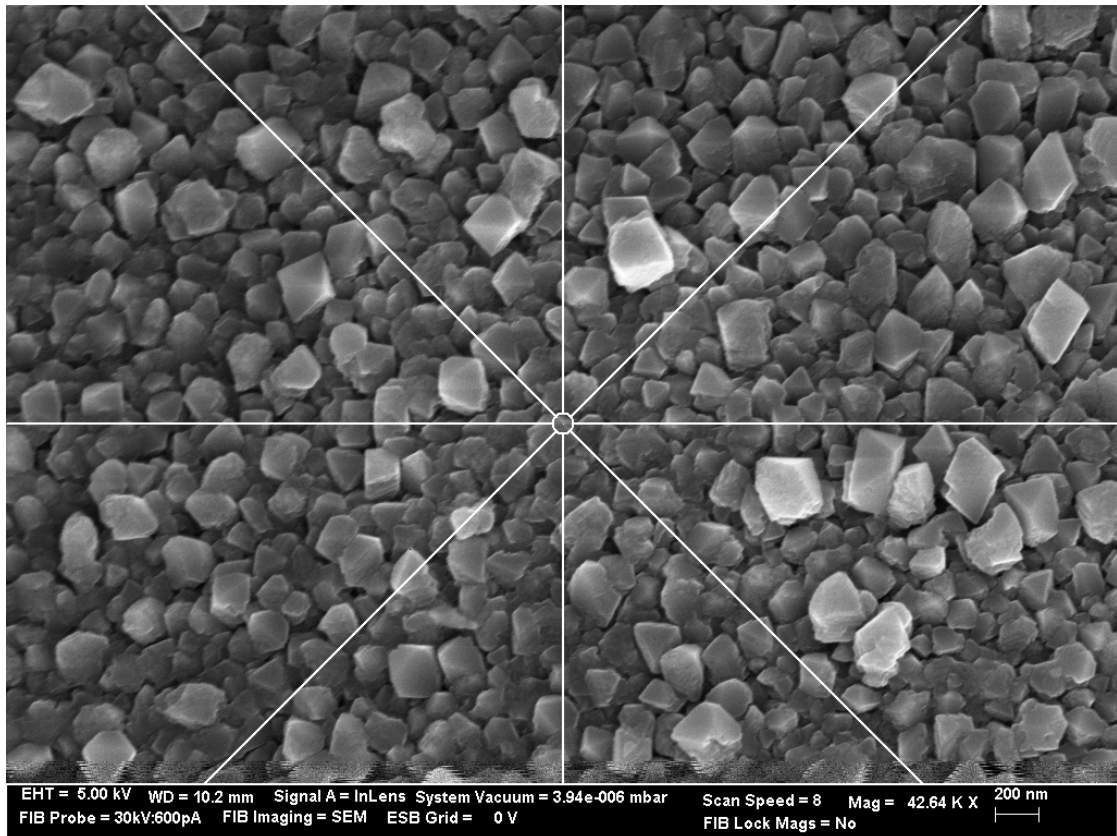


Figure 4.22: Surface morphology of a 24 hour Aluminum deposition on HDPE

This SEM image of the surface of an HDPE microsphere with 24 hours of Aluminum deposition shows a very rough surface with chunks of material of about 200nm in size.

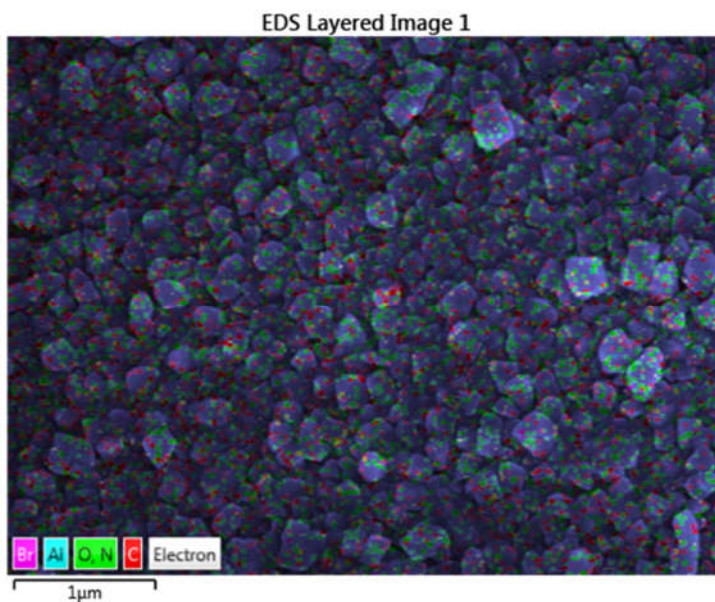


Figure 4.23: EDS of 24 hour Aluminum deposition on HDPE

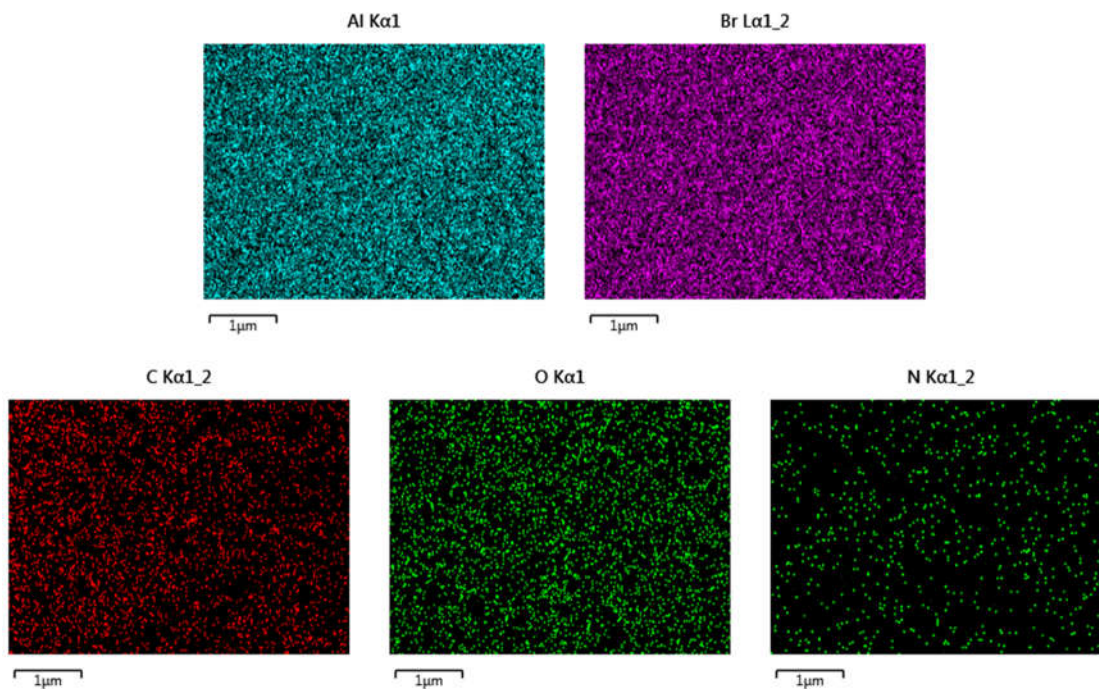


Figure 4.24: EDS of detected elements on sample #6

EDS detected Aluminum, Bromine, Carbon, Oxygen and traces of Nitrogen. While Aluminum is expected, Bromine is not. One of Bromine's critical excitation energies, $L\alpha$ 1.480keV, is actually fairly close to Aluminum's, $K\alpha$ 1.486keV. This may have caused a false detection by the EDS equipment. Other traces are Carbon, which, aligns with the fact the HDPE is a hydrocarbon chain, and Oxygen and Nitrogen with significantly less concentrations.

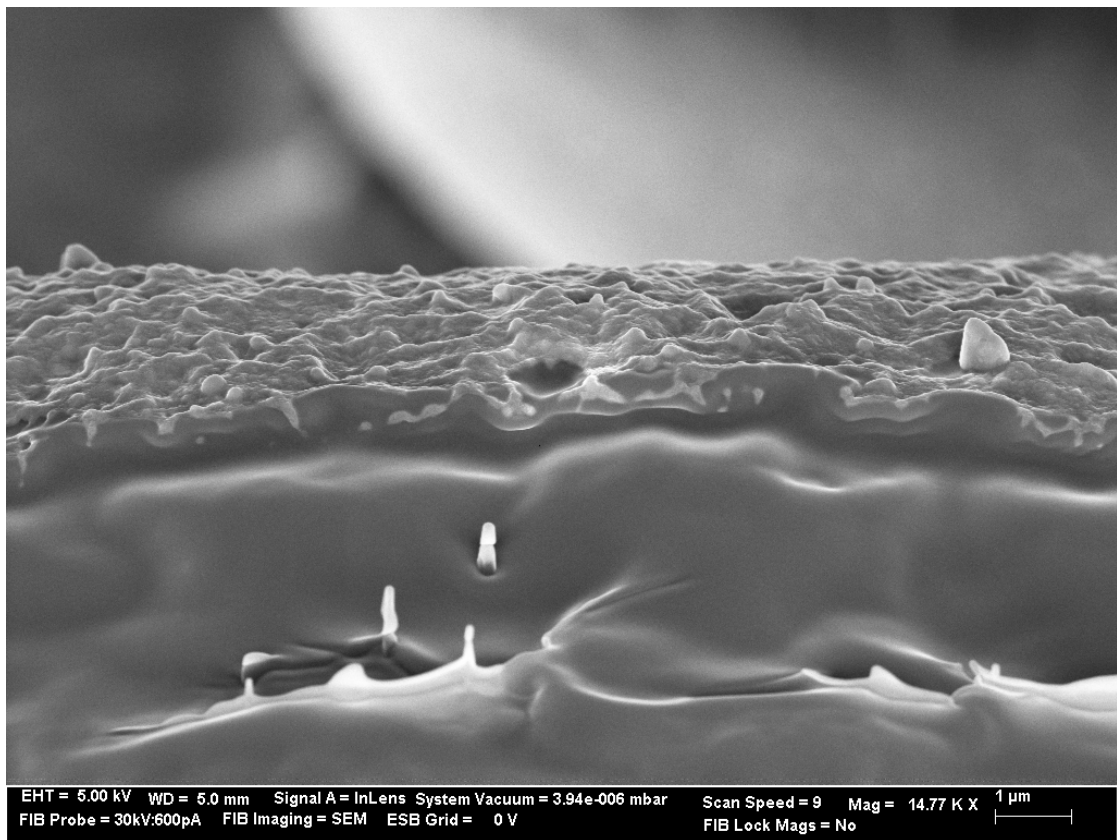


Figure 4.25: SEM of 24 hour Aluminum coating on HDPE microthene sphere cross section

EDS Layered Image 1

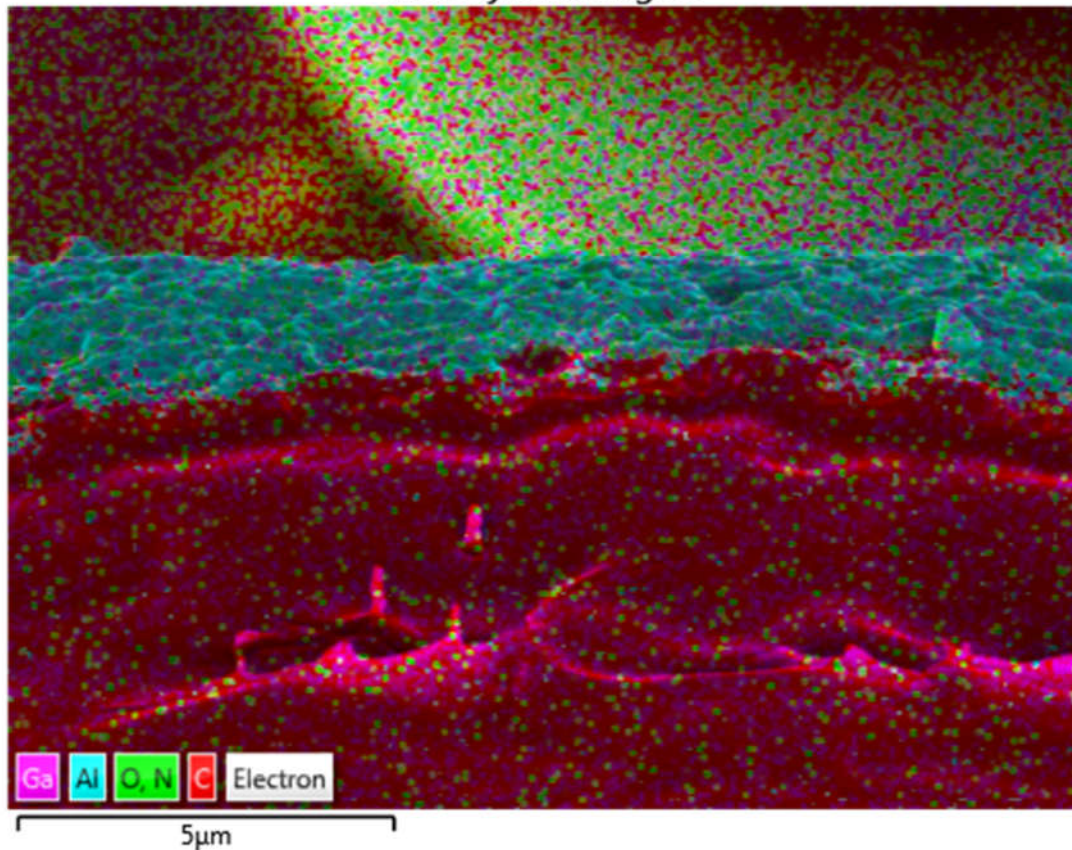


Figure 4.26: EDS of 24 hour Aluminum coating on HDPE microthene sphere cross section

Cross sectional images of the microsphere were taken by again utilizing the FIB. Milling fine features such as thin layers poses the challenge of completely milling away the deposited layer before one is actually able to measure it. When using the FIB it is necessary to turn on the FIB gun before milling in order to ensure that the SEM and FIB are aligned by checking the focusing both the SEM imaging and FIB imaging functions. While the FIB is on for imaging, it is also consequently milling. It is important to take note that this occurs and techniques of waiting for the last possible

moment to turn on the FIB gun and choosing the milling parameters quickly were practiced to lessen the effect of erosion of the sections of the sample that were not intended to be milled. This unintentional milling is visible in the figure above. The rounded features on the top facing side of the sphere indicate some milling. However, there is clearly an enduring Aluminum layer on the surface exposed by EDS mapping. Carbon is detected within the HDPE substrate. There is also a false reading of Gallium within the substrate, this may be due to the fact that this image was taken slightly closer at 5mm, rather than the recommended distance of 8mm.

4.4.3 nanoComposix Generated Mass Extinction Spectrum Profiles

Collected data was reported in absorbance. Beginning with the intensity transmitted

$$I = I_0 e^{-\alpha x} \quad (4.1)$$

Where I is the transmitted intensity, I_0 is the incident intensity, α is the linear absorption coefficient in units of inverse meters, and x is the thickness of the material in units of meters. This is related to an equation in terms of mass concentration as

$$T = \frac{I}{I_0} = e^{-\alpha_{MEC} CL} \quad (4.2)$$

Where α_{MEC} is the mass extinction coefficient in units of m^2/g , C is the mass concentration in units of g/m^3 , and L is the path length through the material in units of m . The optical density (OD) or absorbance (A), unit less, is defined according, again, to Beer-Lambert law as

$$A = -\log_{10} \left(\frac{I}{I_0} \right) \quad (4.3)$$

Where 1OD corresponds to 10dB optical loss [Sigel]. Absorbance and mass extinction coefficient are related by

$$\alpha_{MEC} = 2.3 \frac{A}{CL} \quad (4.4)$$

The value of “2.3” arises from a log base transformation within the derivation.

Values for mass concentration and path length were reported along with raw absorbance data sets for each samples, the mass extinction coefficient was then found. The data collected by nanoComposix engineers was done on two pieces of equipment. The first measurement instrument was a NIR Jasco V670, which collected spectral information for wavelengths from 0.9 μ m to 2.5 μ m. The second instrument utilized was a FTIR Jasco 480 Plus, which collected spectral information for wavelengths from 2.5 μ m to 15 μ m. The same samples were reused for each of the measuring instruments.

Table 4.3: Aluminum study parameters (nanoComposix provided)

Sample #	Path Length (mm)	Mass Sample (g)	Mass KCl pellet (g)	Volume (m³)	Mass Concentration (g/m³)
1	0.415	0.0011	0.102	5.257E-8	20924.12
2	0.375	0.0011	0.1067	7.788E-8	22972.25
3	0.48	0.0018	0.1076	6.0804E-8	29602.88
4	0.404	0.00562	0.10434	5.1178E-8	12783.00
5	0.415	0.0018	0.1104	5.2571E-8	34239.47
6	0.420	0.0010	0.1096	5.3204E-8	18795.48

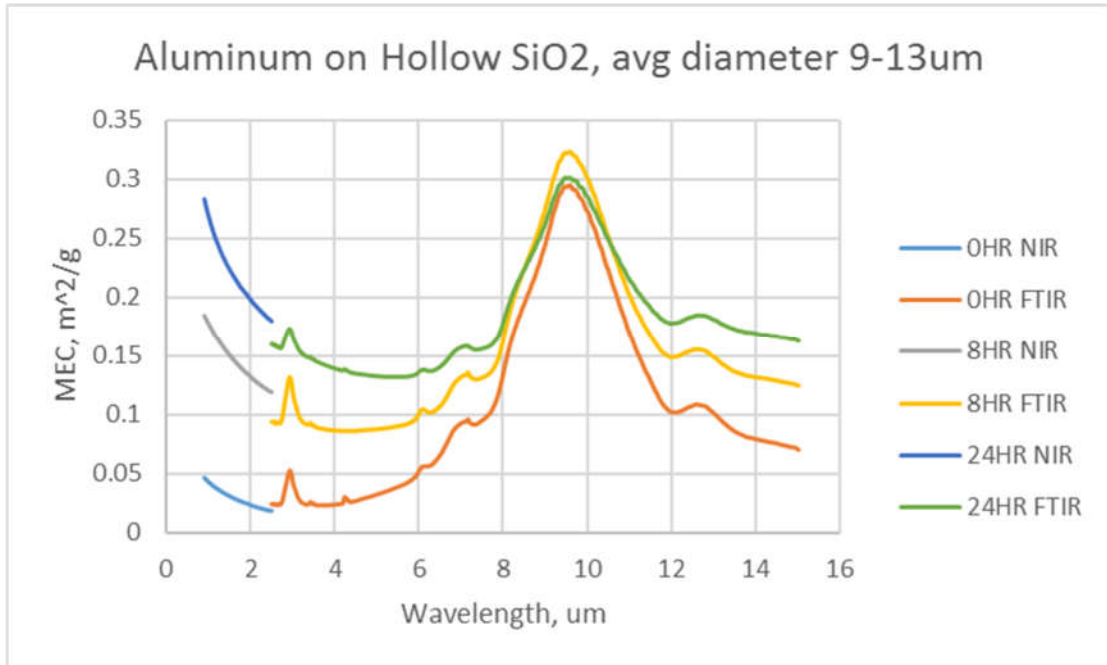


Figure 4.27: Timed Aluminum deposition onto hollow SiO₂ microspheres

This first figure shows the overlaid mass extinction coefficient (MEC) versus wavelength information from the NIR and FTIR measuring instruments for hollow glass microspheres of average diameter 9 μm to 13 μm ; uncoated, 8 hours, and 24 hours of Aluminum deposition. The first feature that draws attention is the huge peak in MEC between 8 μm and 12 μm . This is due to the intrinsic absorptive nature of SiO₂. Recalling Figure 2.6, the imaginary component, k , of the index of refraction of SiO₂ dramatically increases between within the region. Observation also reveals that for most wavelengths more time of Aluminum deposition increases the overall mass extinction coefficient, the only exception is where the “8HR” line surpasses the “24HR” line in that 8 to 12 μm region.

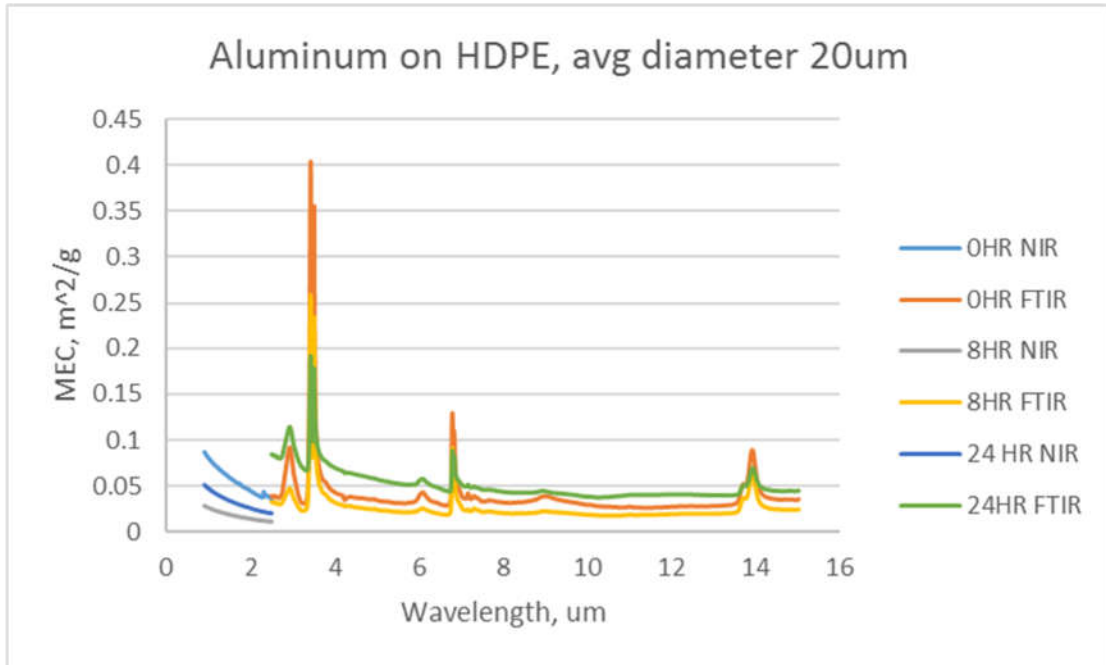


Figure 4.28: MEC of timed Aluminum deposited onto HDPE microthene microspheres

This figure displays the overlaid mass extinction coefficient vs wavelength data for timed Aluminum deposition on to HDPE microthene microspheres of average diameter of 20 μ m. Again, information consists of six samples from two instruments each covering different wavelength regions. In this case, attention is immediately drawn to the huge peaks in mass extinction coefficient at around 3.5 μ m, 6.9 μ m, and 14.2 μ m. These peaks in mass extinction align closely with peaks in absorption for polyethylene verified through Gulmine’s characterization of HDPE [19]. The second most concerning trend is that the curves from the two pieces of equipment do not align and are out of order in terms of mass extinction versus time of deposition. The plots show that the “24HR FTIR” curve possesses the highest mass extinction coefficient values but following is the “0HR FTIR” curve then followed by the “8HR FTIR”

curve. In the NIR there is a similar discrepancy, where instead the “0HR NIR” curve is the highest, but then the next highest is the “24HR NIR” curve then followed by the “8HR NIR” as again the lowest in mass extinction.

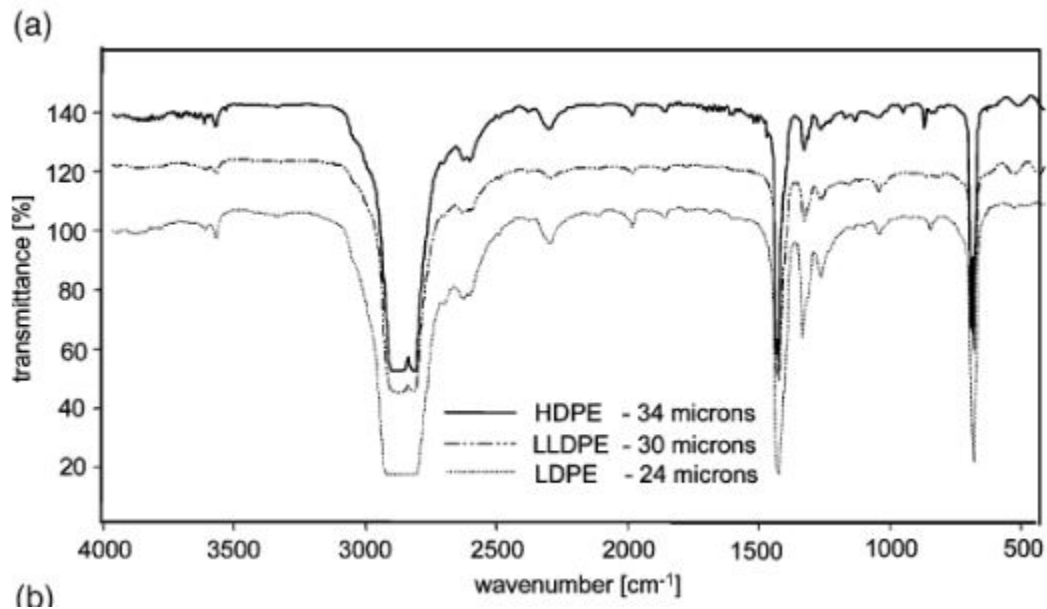


Figure 4.29: Polyethylene transmission spectrum sourced from [19] for comparison to engineered particles

These results indicate that the amount of Aluminum may have made some difference in the spectral analysis between uncoated and aluminum coated spherical substrates but the trends cannot be made and no real interpolation scheme can be incorporated from this data set. Aluminum coating seemed to make a more coherent and pronounced impact when sputtered onto SiO₂ over on to HDPE. This may be the result of not enough even deposition throughout the sample. Through scanning

electron microscopy (SEM) imaging it is evident that not only are the substrates nonuniform but also are the deposited layers from sphere to sphere.

Chapter 5

CONCLUSION AND FUTURE DIRECTION

5.1 Summary

The research conducted throughout this thesis resulted in a novel method of fabricating optical filters based on stratified micro spherical for use within the SWIR and LWIR wavelength regimes. Radio frequency magnetron sputtering was utilized to deposit select materials on to a fluidized bed of micro particles. Though yet not perfected and has struggled to build narrow band pass filters in the SWIR this method has serious potential to build highly extinctive band stop filters for within LWIR. Characterization results have shown that deposition of Aluminum on to certain substrates may have an effect on the mass extinction coefficient's spectral response. Scanning electron and energy dispersive microscopy techniques have been utilized to evaluate films onto various substrates of interest.

5.2 Future Works

Future progress to be made related to this project include running longer depositions, at varying pressures, varying RF source power levels, and to reduce the amount of sample from five grams to an amount such as one or even half a gram at a time to maximize layer thickness and uniformity throughout the entire sample for testing purposes. Further future work includes increasing scale of production by the addition of multiple sputter sources atop the main vacuum chamber of the Denton system or purposing of a larger system with many more sources with larger particle beds to produce larger batches of optical filtering microspheres. If perfected and up scaled this method has great potential for industry and research applications.

REFERENCES

1. Macleod, H. A. *Thin-film optical filters*. Boca Raton, FL: CRC Press/Taylor & Francis, 2010. Web. 6 Apr. 2017.
2. Orfanidis, Socrates J. *Electromagnetic Waves and Antennas*. N.p.: Rutgers U, 2016. Print.
3. Surjikov, S. T. "MIE SCATTERING." *THERMOPEDIA™*. N.p., 14 Feb. 2011. Web. 06 Apr. 2017.
4. Ng, L.N., 2000. *Manipulation of particles on optical waveguides* (Doctoral dissertation, University of Southampton, Faculty of Engineering and Applied Science).
5. J.C. Owrutsky, D.A. Steinhurst, H.D. Ladouceur, H.H. Nelson, A.P. Baronavski, "Obscurants for Infrared Countermeasures III," 2001
6. Brooks Automation, Inc. *Cryo-Torr Pump Installation, Operation and Maintenance Manual*. N.p.: Brooks Automation, 2013. *Brooks Accelerating Innovation*. Web. 6 Apr. 2017.
7. Bohren, Craig F., and Donald R. Huffman. *Absorption and Scattering of Light by Small Particles*. New York: Wiley-Interscience Publication, 1983.
8. Handbook of Optical Constants of Solids, Edward D. Palik, ed. Academic Press, Boston, 1985
9. Pierce, D. T., and W. E. Spicer. "Optical constants of Si (Silicon)Pierce and Spicer 1972: α -Si; n,k 0.01033-2.066 μm ." *RefractiveIndex.INFO*. N.p., 2016. Web. 06 Apr. 2017.
10. Philipp, H. R. "35. Silicon Dioxide (SiO₂) (Glass)." *Handbook of Optical Constants of Solids*. By Edward D. Palik. Vol. 1. San Diego: Academic, 1998. 749-63. Knovel, 07 June 2007. Web. 29 Mar. 2017.
11. Visser, J. "Van Der Waals and Other Cohesive Forces Affecting Powder Fluidization." *Powder Technology* 58.1 (1989): 1-10. Web.
12. Hamaker, H. C. "The London-van Der Waals Attraction between Spherical Particles." *Physica* IV.10 (1937): 1058-072. *The London-van Der Waals Attraction between Spherical Particles - ScienceDirect*. Web. 24 Mar. 2017.
13. Kurt J. Lesker Company. "Indium Target Bonding Service." *Kurt J. Lesker Company*. N.p., 2017. Web. 06 Apr. 2017.

14. Burak Ucer, K. "Sputtering." *Sputtering (cont.) and Other Plasma Processes* *Sputtering Summary* (n.d.): n. pag. *NAN 242 - Thin Film Fabrication*. Wake Forest University, Reynolda Campus. Web. 27 Mar. 2017.
15. Hughes, Matt. "What Is RF Sputtering?" *Semicore*. Semicore Equipment, Inc., 27 Oct. 2016. Web. 27 Mar. 2017.
16. "Materials & Manufacturing (MM) | Ac - Sputtering." *Penn State Applied Research Laboratory*. N.p., n.d. Web. 27 Mar. 2017.
17. Balanis, Constantine A. *Advanced Engineering Electromagnetics*. 2nd ed. Hoboken, N.J: John Wiley & Sons, 2012. Print.
18. Sigel, George H., Jr. "Optical Absorption of Glasses." *Glass I: Interaction with Electromagnetic Radiation*. By Minoru Tomozawa and Robert H. Doremus. Vol. 12. New York: Academic, 1977. 6-7. Print.
19. Gulmine, J. V., P. R. Janissek, H. M. Heise, and L. Akecelrud. "Polyethylene Characterization by FTIR." *Polymer Testing* 21 (2002): 557-63. *ResearchGate.net*. Web. 30 Mar. 2017.
20. "Scanning Electron Microscopy (SEM)." *AAPG Wiki*. Apache, 1 Dec. 2015. Web. 31 Mar. 2017.
21. Jeol. "Energy table for EDS analysis." *Service of Electronic microscopy*. Universite de Namur, n.d. Web. 6 Apr. 2017.
<<https://www.unamur.be/services/microscopie/sme-documents/Energy-20table-20for-20EDS-20analysis-1.pdf>>.
22. "Introduction to Energy Dispersive X-Ray Spectrometry (EDS)." (n.d.): n. pag. *Central Facility for Advanced Microscopy and Microanalysis*. University of California, Riverside. Web. 3 Apr. 2017.